Simulation of Spike Stall Inception in a Radial Vaned Diffuser

by

Raymond Andrew Hill IV

S.B., Massachusetts Institute of Technology (2005)

Submitted to the Department of Aeronautics and Astronautics
in partial fulfillment of the requirements for the degree of

Master of Science in Aerospace Engineering

at the

MASSACHUSETTS INSTITUTE OF TECHNOLOGY

September 2007

Author .....
Department of Aeronautics and Astronautics
August 31, 2007

Certified by .....
Zoltán S. Spakovszky
H.N. Slater Associate Professor of Aeronautics and Astronautics
Thesis Supervisor

Accepted by .....
David L. Darmofal
Associate Professor of Aeronautics and Astronautics
Chair, Committee on Graduate Students

Simulation of Spike Stall Inception

in a Radial Vaned Diffuser

by

Raymond Andrew Hill IV

Submitted to the Department of Aeronautics and Astronautics
on August 31, 2007, in partial fulfillment of the
requirements for the degree of
Master of Science in Aerospace Engineering

Abstract

In turbocharger application bleed air at impeller exit is typically used to seal bearing compartments and to balance axial thrust in the rotor. It was previously shown that this bleed air can have a significant impact on both compressor performance and stability. Experiments suggest that spike stall inception in centrifugal compressors can be formed by a vaned diffuser. To address these issues, a numerical study on an advanced, vaned-diffuser centrifugal compressor was conducted to investigate stall inception. A steady three-dimensional Reynolds-averaged Navier-Stokes simulation using a mixing plane was carried out first to evaluate the effects of bleed air at impeller exit on stage and diffuser subcomponent performance. The steady simulation was compared with experimental measurements and did not show significant changes in stage and subcomponent performance due to leakage flow as observed in the experiments, indicating the importance of unsteady flow effects in the vaneless space and adjacent bleed cavity.

Next, an unsteady three-dimensional Reynolds-averaged Navier-stokes simulation was carried out on four vaned diffuser passages to investigate the response of the diffuser flow field to short wavelength inlet disturbances in total pressure. The simulation employed a new approach, using circumferentially-averaged diffuser inlet conditions obtained from the steady stage simulation, eliminating the impeller and significantly reducing the computational time. This method was capable of simulating spike-like stall precursors rotating at 66% rotor speed which formed in response to inlet flow disturbances. The results represent a first numerical simulation of rotating spike-like flow disturbances in a radial vaned diffuser, and suggest that the spike stall precursors are formed by the vaned diffuser in absence of a tip leakage flow as it can occur in the rotors of axial compressors.

Thesis Supervisor: Zoltán S. Spakovszky
Title: H.N. Slater Associate Professor of Aeronautics and Astronautics

Acknowledgments

This thesis was made possible and supported by ABB Turbo Systems Ltd. under the supervision of Dr. C. H. Roduner. I would first like to thank Dr. Roduner, Niklas Sievers, Jan-Peter Kuhnel, and Hans-Peter Dickmann at ABB for their support, insight, patience, and occasional tricky questions.

I would especially like to thank Professor Zoltán Spakovszky for taking me on this project and for his guidance and leadership. A firm believer in entropy, his passion for the subjects of thermodynamics and turbomachinery have helped me to be a better engineer and researcher. Also in the Gas Turbine Lab, Professor Edward Greitzer was instrumental in helping me expand my understanding of internal and compressible flows. I am also thankful that he told me to get better grades about five years ago, after my freshman year. I would also like to thank Dr. Choon Tan, who was always available for a question and discussion. I appreciate the help and assistance of Lori Martinez, Holly Anderson, and Diana Park in making the wheels of this lab turn. I would also like to thank Alain Demeulenaere, Jean-Charles Bonaccorsi, and especially Roque López at Numeca USA for their very patient assistance with a demanding customer.

Back to the Gas Turbine Lab, my fellow students were a great help in helping me get by. I especially appreciate the camaraderie and advice of office-mates Francois, Barbara, Dave, and Ryan. I also want to thank George for his friendship through TAing, fluids classes, and in the lab. Kip and Pranay are also thanked for their help in making the computers work better. I know the "Numeca Team" is left in good hands.

I want to thank my parents for their support, understanding, and advice through the past two years of graduate school. And last but most certainly not least, Christina has my endless love and gratitude for her understanding, support, time, and encouragement especially over the past two years.

Contents

List of Figures

Nomenclature

α	absolute flow angle
ΔS	discrete surface area differential
Δ	change in quantity
δ^*	boundary layer displacement thickness
η	normal vorticity
π	stage total pressure ratio
ρ	density
$\vec{n}$	surface unit normal vector
$\vec{V}$	velocity vector in absolute frame
ξ	streamwise vorticity
$_{up}$, $_{down}$	quantities upstream and downstream of the mixing plane
$_{E}$	free-stream quantity
$_{r}$, $_{\theta}$, $_{z}$	radial, circumferential, and axial coordinates
$_{max}$	maximum value
A	flow cross-sectional area
a_0	ambient speed of sound

B blockage

c_{leak}, c_{π}, c_{stage} empirical bleed slot constants

$d()$ differential

F mixing plane flux quantity

H static enthalpy

M_{tip} impeller blade tip Mach number

p static pressure

p_T total or stagnation pressure

p_{ref} reference pressure

T_T total or stagnation temperature

T_{ref} reference temperature

u velocity magnitude

U_2 impeller blade tip speed

PS, SS pressure side, suction side

Chapter 1

Introduction

1.1 Background

High-performance turbocharger compressors pose a design challenge in the balance of high pressure rise with a broad operating range and low cost. Recent trends, as reported by Spakovszky and Roduner [20], have moved towards replacing titanium designs, capable of added stability through increased impeller backsweep and increased rotation speed, with aluminum designs because of their significantly lower machining costs. This motivates an improved understanding of the complex flow phenomena present in centrifugal compressors in order to gain a better understanding of the mechanisms limiting the stability of centrifugal compression systems.

Centrifugal compressors, unlike axial compressors, gain much of their pressure rise and work input through the centrifugal effects in the impeller. This allows a much higher single-stage pressure ratio compared to axial compressors, and pressure ratios as high as 12 have been reported in the literature [23]. Like axial flow compressors, however, centrifugal compressors are limited in their performance by two forms of instabilities: rotating stall and surge. Surge is a one-dimensional, system–scale phenomenon, where the compression system experiences reversed flow and a substantial loss in pressure rise. The frequency of these oscillations is usually several Hertz. Rotating stall is a three-dimensional phenomenon, where cells of stalled flow rotate around the annulus at a fraction of the rotor frequency. Rotating stall can, and often

does, lead to surge, as first reported by Emmons et al. [5].

From an operational standpoint, summarized for example in Cumpsty [2], as mass flow is reduced in the compression system the pressure rise increases to a point generally referred to as the "surge point" where the flow field departs abruptly from its steady axisymmetric behavior and experiences rotating stall, surge, or both phenomena. Stall and surge can lead to serious consequences in compressor operation, such as blade breakage, fatigue, and overheating or complete loss of power in a gas turbine application.

Pre-stall behavior, or stall inception, as it will be referred to here, comprises the path into compression system instability. A useful description and summary of the phenomena can be found in Camp and Day [1]. Short-wavelength, or "spike" stall inception consists of flow field perturbations on the blade-scale which propagate around the circumference, growing in size to become a fully-developed rotating stall cell. Long-wavelength, or "modal" stall inception is a radius-scale phenomenon, comprised of wave-like perturbations occupying a larger extent of the circumference. Modal waves form and can grow to cause a spike or a rotating stall cell [1]. This thesis focuses on the mechanisms and the necessary flow conditions for spikes to occur in centrifugal compressors.

Radial diffusers are found in two general forms: vaned and vaneless. Vaned diffusers are more commonly used in high-performance centrifugal compressors where high efficiency and pressure recovery are of primary concern [2]. Vaned diffusers also achieve the higher pressure recovery at a smaller exit radius then the vaneless type [6]. A vaneless diffuser, however, is less expensive to manufacture and has a wider stable operating range [2].

Extensive research has been conducted on stall and surge, beginning with the seminal work of Emmons et al. [5], which showed that rotating stall can precede surge in centrifugal compressors. An early attempt at establishing a linear model and criteria for determining system stability was made by Stenning [22]. The work of Stenning analyzed the dynamic stability of the compression system using the pressure rise characteristics of the system, and presented simple criteria to predict stability. The model

outlined by Moore and Greitzer [14] demonstrated that post-stall transients are the mature, or fully-developed, forms of small perturbations, which are the natural oscillations of the compression system. Their model predicted modal stall waves in axial compression systems, which were later identified in experiment by McDougall et al. [13] and by Camp and Day [1].

Specifically in vaned-diffuser centrifugal compressors, investigations have been performed to investigate the stability of the various diffuser sub-components, beginning with Dean [4] and much later by Hunziker and Gyarmathy [10]. These investigations and others identified the semi-vaneless space as the most critical, or limiting, element of the compressor stage. Spakovszky [19] made the first observation of backward-traveling modal waves leading to system instability in a vaned-diffuser centrifugal compressor, which were most dominant near the diffuser throat.

Spakovszky and Roduner [20] investigated a centrifugal compressor which exhibited a 50% loss in stable flow range when leakage flow was bled from the impeller exit simulating a turbocharger environment. When leakage flow, used for secondary flow systems, was bled from the impeller exit, the compressor experienced modal stall inception, which was suggested to occur due to a redistribution of the diffuser subcomponent loading caused by endwall flow leakage in the vaneless space between impeller and diffuser. The endwall flow leakage modifies the dynamic behavior of the diffuser subcomponents, which changes the form of stall inception from spikes to modal waves. Their results comprise a first measurement of spikes in a centrifugal compressor, and suggest that spikes are formed by the diffuser. The research in this thesis is motivated by their suggestion that the vaneless space and vaned diffuser are the key components contributing to compressor stability.

In the past ten to fifteen years, computational fluid dynamics (CFD) has been used extensively in compressor research. For example Dawes [3] performed a time-accurate calculation on a vaned-diffuser centrifugal compressor. Dawes' results suggest the axial, or spanwise, non-uniformities in the flow exiting the impeller had the greatest influence on the diffuser performance. Dawes concludes that high losses in the diffuser are attributed to a hub-corner stall initiated by the spanwise distortion in flow angle.

Stein et. al [21] simulated stall and surge in a vaneless-diffuser centrifugal compressor using a time-accurate calculation. Their analysis concluded that surge was triggered by unsteady vortex shedding phenomena and boundary layer separation at the impeller blade leading edge. Finally, Peeters and Sleiman [16] performed steady and unsteady simulations of a vaned-diffuser centrifugal compressor, and identified several shortcomings of a steady simulation. They demonstrated that the mixing plane eliminated the upstream influence of the diffuser, with the exception of setting the pressure level at the interface. In addition, their results indicated an unrealistically low static pressure recovery in a vaned diffuser in a steady simulation. Shortcomings specifically regarding the mixing plane approach will be discussed in Chapter 2.

1.2 Motivation

As stated above, the recent work by Spakovszky and Roduner [20] demonstrated two forms of stall inception in the same advanced, pre-production, turbocharger compressor and presented the first measurement of spike stall inception in a centrifugal compressor with a vaned diffuser. When leakage flow is bled from the impeller, the form of stall inception changes from spikes to modal waves. The leakage flow, used in turbocharger applications to seal the bearing compartment and to provide compensation for the axial thrust in the turbocharger, amounts to approximately 0.5% of inlet mass flow. Figure 1-1 illustrates the location of the leakage flow, identified as the annular bleed slot, and a general schematic of the compression system. When leakage flow is present, flow stability is limited by modal waves, resulting in a 50% loss in stable operating range, as shown in Figure 1-2. The investigation suggests that the leakage flow modifies the interaction of viscous endwall and inviscid core flow in the vaneless and semi-vaneless space of the diffuser. This leads to a redistribution of diffuser subcomponent loading and a re-matching of the components in the diffuser, which changes the compressor dynamic behavior and the form of stall inception.

Figure 1-3 shows the static pressures measured on an array of unsteady pressure transducers in the vaneless space in experiments performed in [20]. The traces show

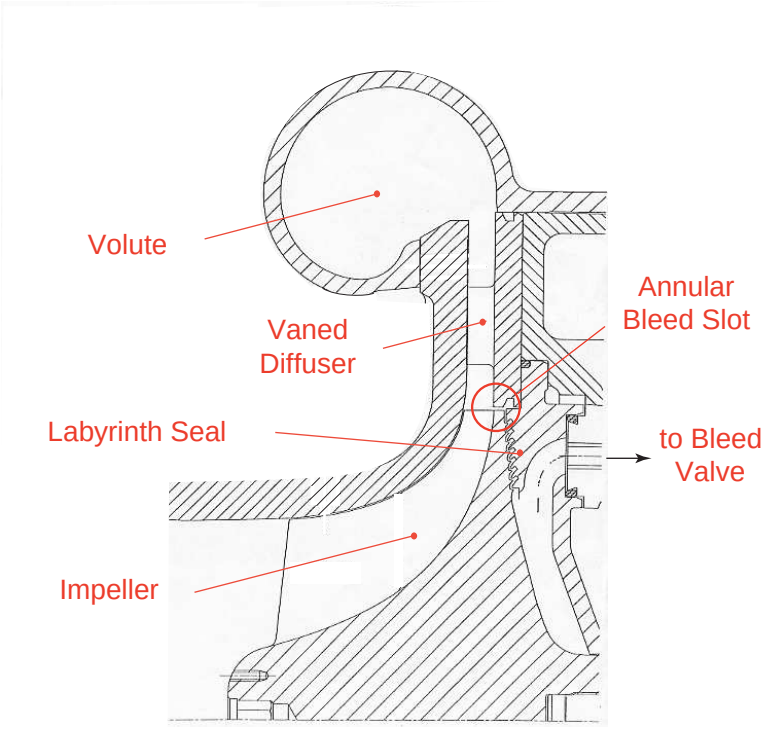

Figure 1-1: High pressure ratio centrifugal compressor of advanced design. Note leakage location at impeller exit. Figure adopted from [20].

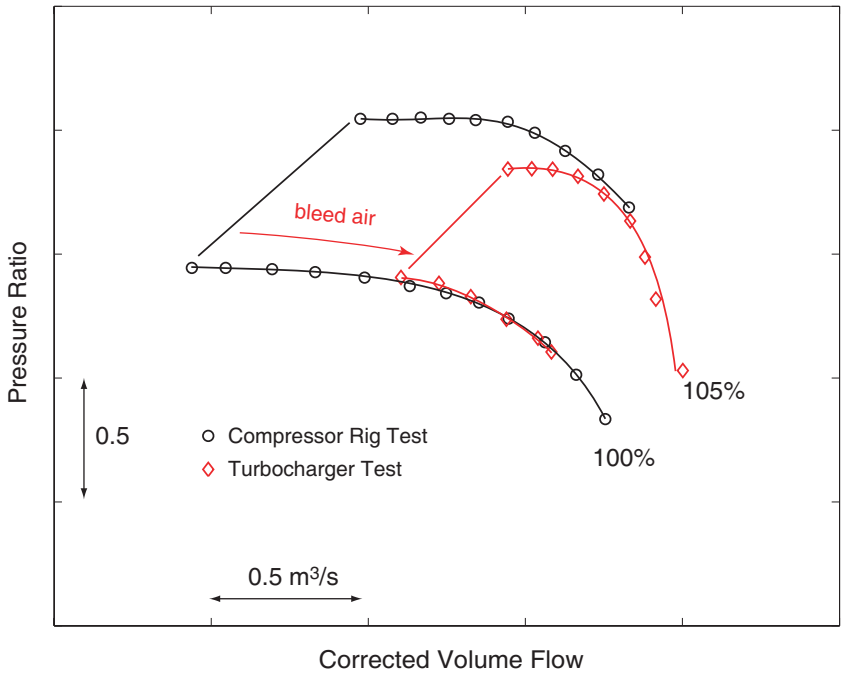

Figure 1-2: Effect of bleed air on compressor performance at 100% and 105% corrected speed; circles: compressor rig test (no bleed); diamonds: turbocharger test (bleed). Figure adopted from [20].

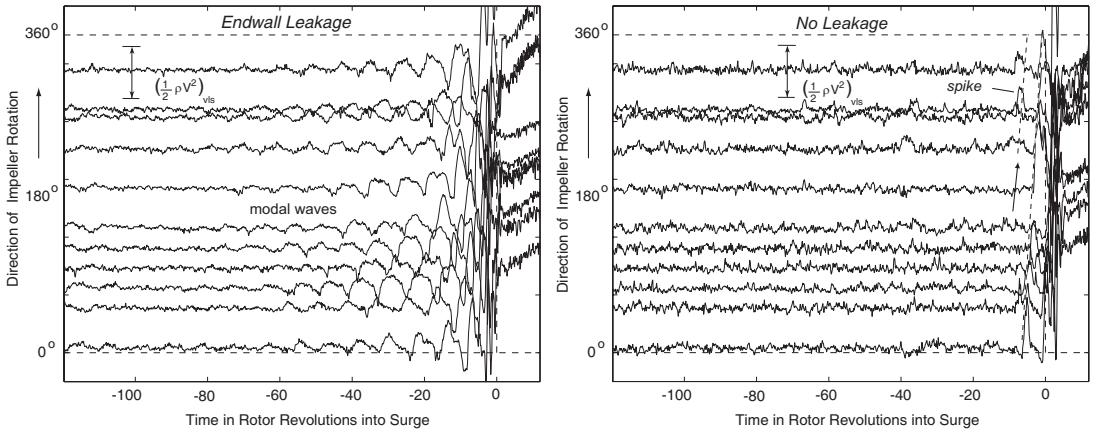

Figure 1-3: Static pressure traces measured in the vaneless space showing spikes (right) and modes (left) driven by the leakage flow. Figure adopted from [20].

the existence of modes and spikes in cases with and without leakage flow.

The experimental observations point towards the influence of non-uniform flow on the stability of the vaneless and semi-vaneless space in a vaned-diffuser centrifugal compressor. The presence of both spikes and modal waves in a vaned-diffuser centrifugal compressor motivates the investigation of the key mechanisms leading to stall precursors.

1.3 Research Questions

Significant work has been performed on the topic of stall precursors, but the paths into instability have not been as thoroughly examined in centrifugal compressors as in axial compressors. In light of the research referenced, the following questions are addressed in this thesis:

- What role does the axial flow non-uniformity play in diffuser subcomponent performance and the stall inception process?
- What are the flow mechanisms that lead to changes in the dynamic behavior of the diffuser components?
- Can multi-passage calculations reproduce phenomena observed in the experiments and capture the underlying mechanisms?

A three-part hypothesis is presented to address these questions: the non-uniform flow in the vaneless space plays a key role in the stable flow limit and path to instability by modifying the performance of vaned diffuser subcomponents; the leakage flow and the presence of a cavity between the impeller and vaned-diffuser significantly modifies the non-uniform flow, and therefore the stable flow limit of the device; it is possible to simulate rotating disturbances with a multi-passage unsteady RANS calculation.

1.4 Technical Roadmap

To evaluate the above hypotheses, numerical computations are carried out in combination with existing experimental measurements. First, a steady, three-dimensional, high-fidelity RANS (Reynolds-averaged Navier-Stokes) simulation of the compressor stage is carried out to model the effects of leakage flow on the stage performance. The calculation attempts to determine if there is a reduction in operating range in the compressor stage due to the leakage flow, and whether there is a redistribution of diffuser subcomponent loading as seen in experiment. In addition, a detailed analysis of the endwall flow behavior in cases with and without leakage flow is carried out. The swirling boundary layer present at the hub endwall and modified by the leakage flow is investigated.

Next, an unsteady, three-dimensional, high-fidelity unsteady simulation of the highly-loaded vaned diffuser is carried out on multiple vane passages using circumferentially–averaged flow conditions obtained from the stage simulation at impeller exit as inlet boundary conditions. The results of these calculations are also compared with existing experimental data. This analysis is used to gain further insight in to the diffuser stability. Eliminating the impeller from the computational domain reduces the computational time and enables a systematic analysis of the effects of flow non-uniformity on stall inception. The potential effects of the impeller hub seal cavity are also discussed and will be addressed in future work.

Finally, a short wavelength perturbation is input for a short time to a portion of the inlet boundary surface of the multi-passage diffuser domain in an unsteady calculation

near the stability limit of the simulated vaned diffuser. The goals of this part of the thesis are to investigate whether short wavelength stall pre-cursors (spikes) evolve, to determine how the flow field breaks down, and to identify sources and mechanisms that initiate stall. A first simulation of rotating spike-like stall precursors in a radial vaned diffuser is presented.

1.5 Contributions

The contributions of this thesis can be summarized as follows:

1. A steady simulation of a centrifugal compressor using a mixing plane technique is evaluated, and the shortcomings in evaluating several flow details are outlined.

2. Further analysis of the steady simulation suggests that the impeller exit cavity must be modeled to model the effects of leakage flow.

3. A first-of-its-kind simulation of rotating stall-like disturbances in a multi-passage diffuser simulation is presented, using a novel approach to reduce complexity and computational time.

Chapter 2

Assessment of Leakage Flow Effects on Compressor Performance

As discussed earlier, previous experiments demonstrated the importance of leakage flow on the operating range and type of stall inception in a high-speed centrifugal compressor with a vaned diffuser [20]. At 100% speed the data show a reduction in operating range and a change from spike to modal stall inception, which is suggested to be driven by a change in subcomponent loading. There is no detailed flow data available to help determine the mechanisms that drive the changes shown in the experiment. Thus high-fidelity three-dimensional CFD simulations are carried out. Past research has shown the difficulties present when simulating blade-row interactions in both axial and centrifugal compressor stages [3] [16], and the decision of how to implement the rotor-stator interface rests on the objective of the calculations and the flow features to be resolved. The most detailed method is to perform a time-accurate calculation and to utilize a sliding mesh. This technique is computationally expensive. An alternative is to perform a steady calculation, using a mixing plane between the rotor and stator. The latter technique was used to produce the results discussed in this chapter.

The first step was to validate the CFD implementation via a consistent comparison of compressor performance with experimental results. Next, the leakage flow implementation was validated by examination of the endwall flow features near the

impeller exit. Finally, the endwall flow features through the vaneless space and the diffuser passage were examined for near-stall operating points both with and without leakage flow. The goal was to determine if the leakage flow extraction reduced the endwall blockage or otherwise modified the non-uniform flow entering the diffuser, which may have an effect on the mechanisms that lead to stall inception. The analysis suggests that the steady calculations have merit in evaluating some flow features efficiently but are not appropriate for examining near-stall behavior. To further investigate the compressor dynamic behavior, unsteady flow simulations of the vaned diffuser only were carried out and are discussed in Chapter 3.

2.1 Description of Numerical Simulations

This section describes the setup of the numerical simulations analyzed later in this chapter. The centrifugal compressor modeled by the CFD software is first described. Next, the features of the CFD software are summarized, followed by a description of the computational grid. Finally, the concept of the mixing plane analysis and its implementation in the simulations is outlined.

2.1.1 Compressor Stage Definition

The compressor stage geometry used in the simulations described in this thesis is identical to the one tested in the experiments in reference [20]. The simulated centrifugal compressor is a pre-production vaned-diffuser turbocharger compressor of pressure ratio 5 and is representative of modern turbocharger compressors of advanced design. The impeller tip Mach number $M_{tip} = U_2/a_0$exceeds unity at 100% design speed. The impeller consists of 9 main and 9 splitter blades, and the diffuser consists of 16 aerodynamically-profiled vanes. Key characteristics of the geometry are summarized in Table 2.1. This particular compressor stage is intended for application in large diesel engines used in heavy industrial equipment.

2.1.2 Flow Solver

The simulations described in this thesis were carried out using Numeca International's FINE/Turbo software package. FINE/Turbo is an integrated software interface designed for turbomachinery. It contains several software interfaces, each tailored to a specific stage of the CFD process. An automatic grid generator, AutoGrid, allows for rapid design of structured numerical grids for complex turbomachinery geometries. FINE (*Flow INtegrated Environment*) is a graphical user interface for the flow solver engine, known as EURANUS. The CFView interface accomplishes the post-processing, and includes python scripting capability for automated post-processing. The software package is capable of steady and unsteady RANS simulations, and algebraic (Baldwin-Lomax), one-equation (Spalart-Almaras), or two-equation (k-ε) turbulence models. In the stage calculations described and analyzed in this chapter, the Spalart-Almaras model is used.

The flow solver makes use of a "multigrid" technique, where nodes are dropped in each direction in which there is an even number of cells. In a three-dimensional mesh, this can result in an eight-fold reduction of the number of cells every time the grid is coarsened, speeding up convergence significantly. Once a converged solution is achieved on the coarse grid, it can be used to initialize the fine grid, which improves the resolution of the calculation. In addition, within each iteration, multiple "sweeps" are made on coarser grids in order to speed convergence. A more detailed discussion of the multigrid technique can be found in [15]. The multigrid capability also improves the stability of the calculation, as a coarse mesh is more capable of diffusing numerically-induced instabilities.

2.1.3 Computational Grid

The pertinent grid characteristics and stage geometry are summarized in Table 2.1.

The numerical grid, created with AutoGrid, includes one main and one splitter blade passage, and one diffuser vane passage. The impeller tip gap mesh used 17 points in the spanwise direction. Each impeller passage grid contained approximately

Stage Geometry		
Impeller blades		18
	Main blades	9
	Splitter blades	9
Diffuser vanes		16
Grid Characteristics		
Spanwise points		
	Impeller	57
	Tip Gap	17
	Diffuser	41
Main blade points		500,000
Splitter blade points		500,000
Diffuser vane points		250,000
	Total grid points	1,250,000
Mixing plane location		107% R_2
Diffuser exit location		163% R_2

Table 2.1: Summary of pertinent grid and stage geometry characteristics

500,000 points, and the diffuser grid contained approximately 250,000 points, for a total grid size of approximately 1.25 million points. The grid was checked for consistency and compared with other speed-line calculations on the same geometry. In addition, the diffuser grid density was increased and decreased by a factor of two with no appreciable changes in stage performance. The numerical grid used for the calculations analyzed in this chapter is depicted in Figures 2-1 and 2-2. The left view shows a projection of the grid on the solid boundaries, and the right view shows the hub and shroud profiles, with key dimensions from Table 2.1 highlighted.

In order to improve convergence characteristics affected by flow separation and reversal at the diffuser trailing edge, a "pinch" was used, as shown in Figure 2-2, at the diffuser exit. Periodic boundary conditions were used at the circumferential boundaries of the combined single-passage stage grid to simulate the full circumference with only a single instance of the main and splitter blades and the diffuser vanes. The impeller hub was assumed to be continuous and gapless at the interface

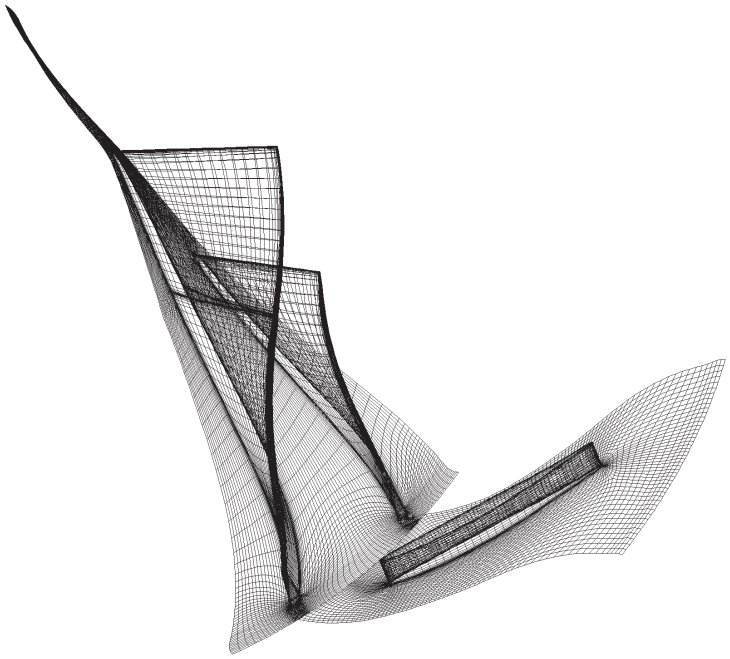

Figure 2-1: Fine mesh projected on solid surfaces. Shroud endwalls not shown for clarity.

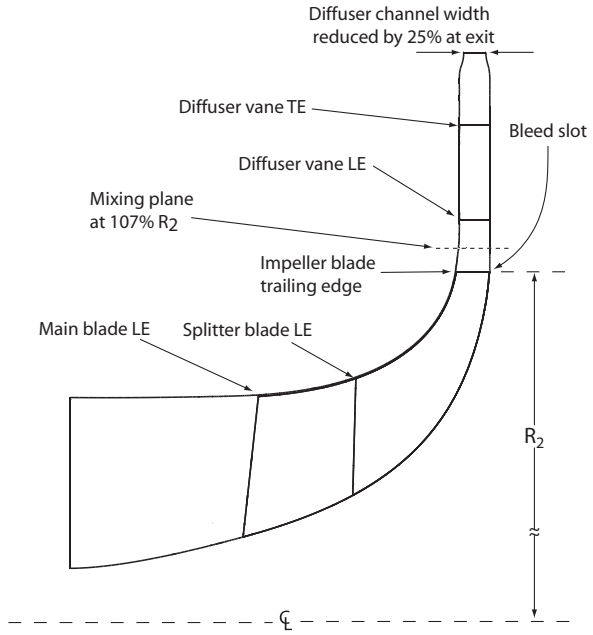

Figure 2-2: Meridional view of computational domain, showing shroud and hub contours and key details of the compressor geometry.

joining rotating and non-rotating hub surfaces at impeller exit, and the bleed flow was simulated by a boundary condition change which will be discussed later.

2.1.4 Mixing Plane Concept

At the boundary between the exit of the impeller computational domain and the inlet of the diffuser computational domain, a mixing plane was used to provide the transmission of information between rotating and non-rotating components. First, on either side of the boundary, flux variables are created based on the mass, momentum, and energy fluxes. The fluxes and the equations used to transfer information across the mixing plane boundary are written below to guide in the discussion regarding several shortcomings of a mixing plane implementation.

$$\begin{aligned} F_1 &= \rho\vec{V} \cdot \vec{n}\Delta S \\ F_2 &= \rho V_r\vec{V} \cdot \vec{n}\Delta S \\ F_3 &= \rho V_\theta\vec{V} \cdot \vec{n}\Delta S \\ F_4 &= \rho V_z\vec{V} \cdot \vec{n}\Delta S \\ F_5 &= \rho H\vec{V} \cdot \vec{n}\Delta S \end{aligned} \tag{2.1}$$

Next, the flux variables and the static pressure are averaged in the circumferential direction. Finally, new values for each local grid point are determined. The upstream flux variables are determined from the local upstream value with the contribution of the downstream circumferentially-averaged static pressure to the radial and axial momentum flux components as shown below.

$$\begin{aligned} F_1^{up} &= F_1^{up} \\ F_2^{up} &= F_2^{up} + \overline{p}^{down} n_r \Delta S \\ F_3^{up} &= F_3^{up} \end{aligned}$$

$$
\begin{aligned}
F_4^{up} &= F_4^{up} + \overline{p}^{down} n_z \Delta S \\
F_5^{up} &= F_5^{up}
\end{aligned}
\tag{2.2}
$$

For the downstream side, the flux variables are determined from the upstream circumferentially-averaged flux variables, indicated by the macron as in $\overline{F}_1$, with the contribution of the local downstream static pressure as shown below.

$$
\begin{aligned}
F_1^{down} &= \overline{F}_1^{up} \\
F_2^{down} &= \overline{F}_2^{up} + p^{down} n_r \Delta S \\
F_3^{down} &= \overline{F}_3^{up} \\
F_4^{down} &= \overline{F}_4^{up} + p^{down} n_z \Delta S \\
F_5^{down} &= \overline{F}_5^{up}
\end{aligned}
\tag{2.3}
$$

The advantage of a mixing plane concept is its efficiency in simulating blade-row interactions with a steady calculation. However, the details of the interaction are not fully accounted for by this implementation. Equation 2.2 shows that the upstream fluxes are unchanged by the downstream flow field except, in the general case, through the radial and axial pressure forces. Specifically in a centrifugal compressor, where $n_z = 0$, only the radial pressure force affects the upstream flow field.

Figure 2-3 shows static pressure coefficient contours and illustrates the pressure gradients in both the radial and tangential directions. Figure 2-3 shows that there is a significant component of the upstream influence of the diffuser vanes in the circumferential direction, which by Equation 2.2 is not carried through the mixing plane to the impeller domain. The potential implications of this omission will be discussed later in this chapter.

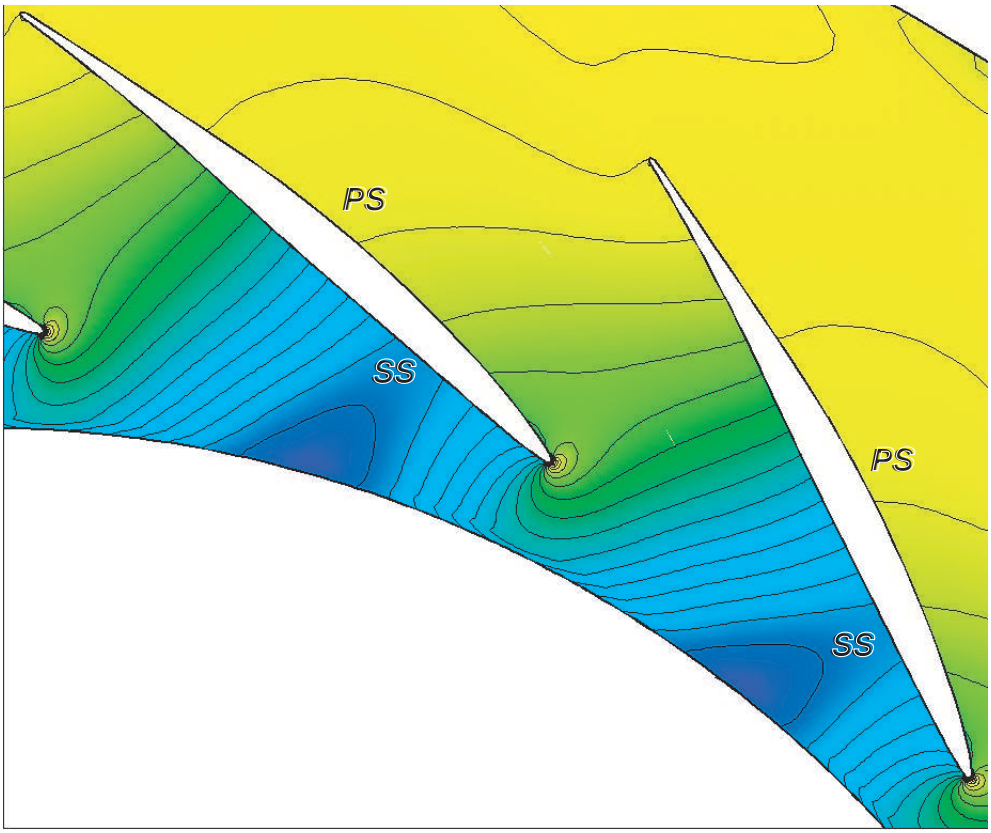

Figure 2-3: Contour of static pressure coefficient (isolines at 0.05 intervals) for an operating point near stall without flow leakage at impeller exit, indicating the direction of the pressure gradient in the semi-vaneless space, influencing the flux variables at the mixing plane.

2.2 Numerical Simulation Procedure

This section outlines the choice of boundary conditions used to define each operating point, specifically addressing the implementation of the leakage flow at impeller exit. Additionally, the initialization of the computations is described.

2.2.1 Boundary Conditions

The boundary conditions were defined as follows: total temperature, total pressure, and axial flow direction were defined at impeller inlet; average static pressure was defined at the diffuser outlet. Solid boundaries were either set to a rotation rate corresponding to 100% corrected rotor speed, or were made stationary. To simulate closing of a throttle, the averaged diffuser exit static pressure was carefully increased through the computational operating range.

This choice of exit boundary condition, while simple to implement, can cause numerical problems near peak pressure rise. In the case discussed here a significantly higher minimum mass flow was observed in the simulation relative to the experiment. The discrepancy in stall point between experiment and simulation is believed to be linked to static and dynamic stability, influenced by the interaction of the exit boundary condition with the stage characteristic. Typical compressor, throttle, and backpressure characteristics are illustrated in Figure 2-4. A compression system is statically stable if the slope of the throttle characteristic is greater than that of the compressor characteristic [7]. The experiments used a physical throttle while the simulation used a fixed exit pressure to simulate a throttle. This does not present a problem near choke, but as the backpressure is increased, the compressor characteristic approaches the zero-slope condition set by the the backpressure characteristic. At this point, the simulated system becomes statically unstable and achieving a stable, converged, equilibrium solution can be difficult. The actual throttle characteristic has a positive slope which allows the compressor to operate to much lower mass flows. A solution to the exit boundary problem is to specify the exit mass flow, but calculations using a specified exit mass flow experienced numerical difficulties and are not

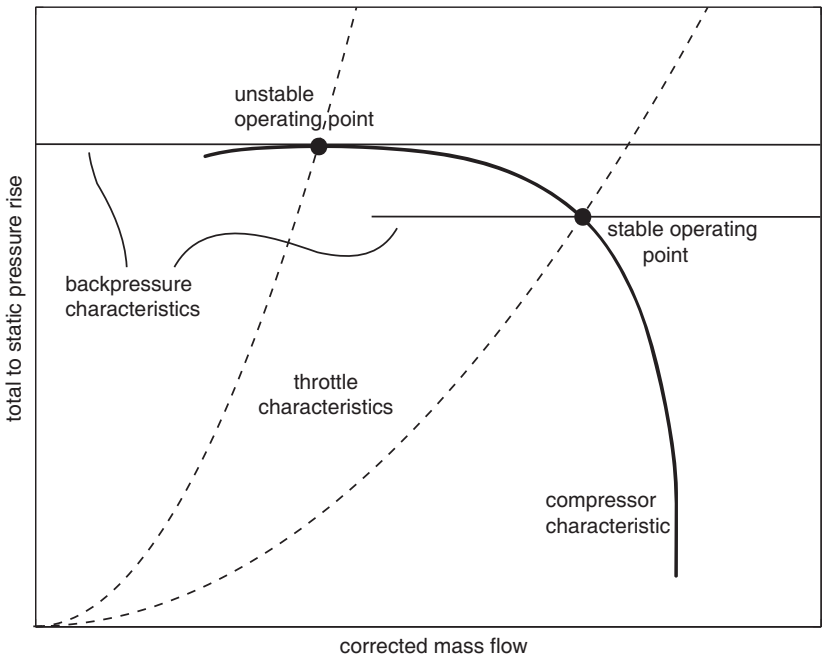

Figure 2-4: Typical throttle, backpressure, and compressor characteristics.

discussed in this thesis.

2.2.2 Application of Leakage Flow at Impeller Exit

Simulating the actual turbocharger environment, the leakage flow was bled from the hub surface at impeller exit by specifying a bleed mass flow. An automated injection/bleed module in the software environment distributes the bleed mass flow across selected hub endwall grid points that lay within the slot area at the impeller exit. Figure 2-5 illustrates the implementation of leakage flow in the FINE/Turbo software environment. Figure 2-5.1 shows the grid cells selected to extract the leakage mass flow, while Figure 2-5.2 shows the resultant momentum flux through the simulated bleed slot. Note that in Figure 2-5.1 the grid points do not follow a circumferential arrangement and the flow solver selects the points that most accurately simulate the bleed slot. It should also be noted that the simulated hub endwall is smooth over the bleed slot, unlike in the actual compressor stage shown in Figure 1-1, where the edge of the physical bleed slot is sharp. The smooth profile helps to procure an efficient and stable calculation, but a source of additional endwall separation and blockage is

omitted from the simulation as a result.

The quantity of leakage flow was obtained from a regression equation derived from experimental measurements and shown below [18].

$$\dot{m}_{leakage} = \frac{p_{Tinlet}}{p_{ref}} \sqrt{\frac{T_{ref}}{T_{Tinlet}}} c_{leak} (\pi - c_{\pi})^{c_{stage}} \tag{2.4}$$

Where c_{leak}, c_{π}, and c_{stage} are constants. The leakage mass flow is approximately 0.5 to 1% of the impeller inlet mass flow. To test the sensitivity of the stage behavior to the simulated leakage mass flow, an additional speed-line calculation was carried out where the amount of leakage flow was doubled. This calculation showed little change in the compressor stage behavior. Additionally, the leakage flow implementation does not entirely capture the nature of the leakage flow in the turbocharger test rig. Figure 2-5.1 shows that the degree of accuracy in approximating the shape of the bleed slot is limited by local grid density. Additionally, there is a cavity between the impeller and diffuser hub surfaces, shown in Figure 1-1, which is not part of the mesh in the calculations described in this thesis. The interaction of a bleed slot with the primary flow has been shown to affect loss characteristics [12], and ongoing numerical work on this compressor will address the issue.

2.2.3 Initialization Procedure and Convergence Criteria

The calculations were initialized from a simplified initial estimate, where the inlet duct, impeller blade, and diffuser domains were set to uniform states. The back-pressure was set to a relatively low value, and the calculation was allowed to run for approximately 800 iterations on the coarse mesh until a reasonably favorable convergence could be achieved. A series of coarse grid calculations was carried out in this manner with gradually increasing backpressures. Each calculation used the previous calculation as an initial solution. These coarse grid solutions were then used to initialize fine grid calculations, which were run until the total inlet and outlet mass-flows, accounting for leakage flow when applicable, were within 0.5% of each other and did not vary by greater than 0.1% over 100 iterations. The calculations were carried

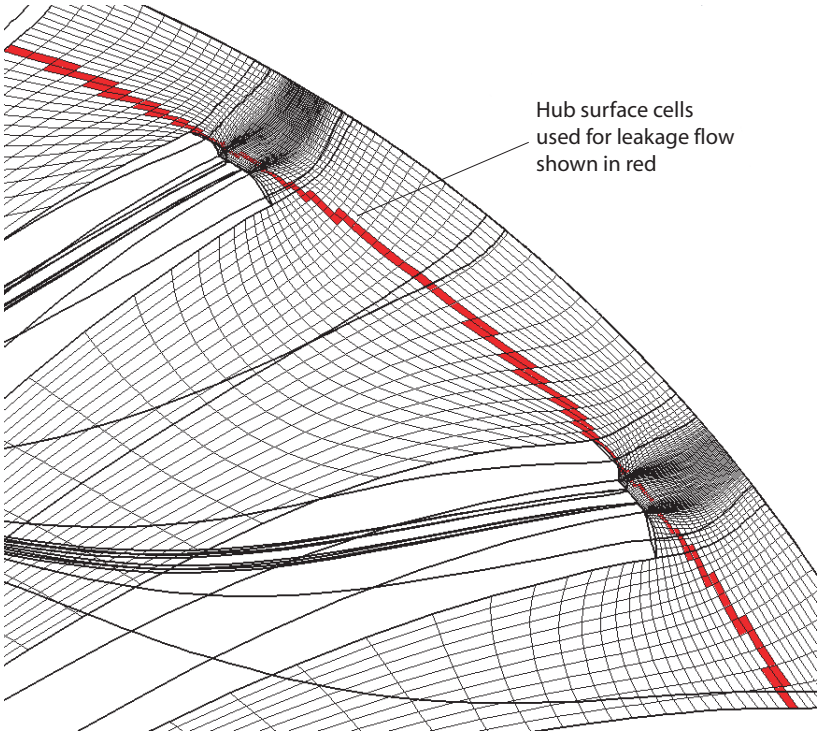

2-5.1: Hub surface of fine mesh, indicating surface cells used for leakage flow as selected by the FINE/Turbo bleed module.

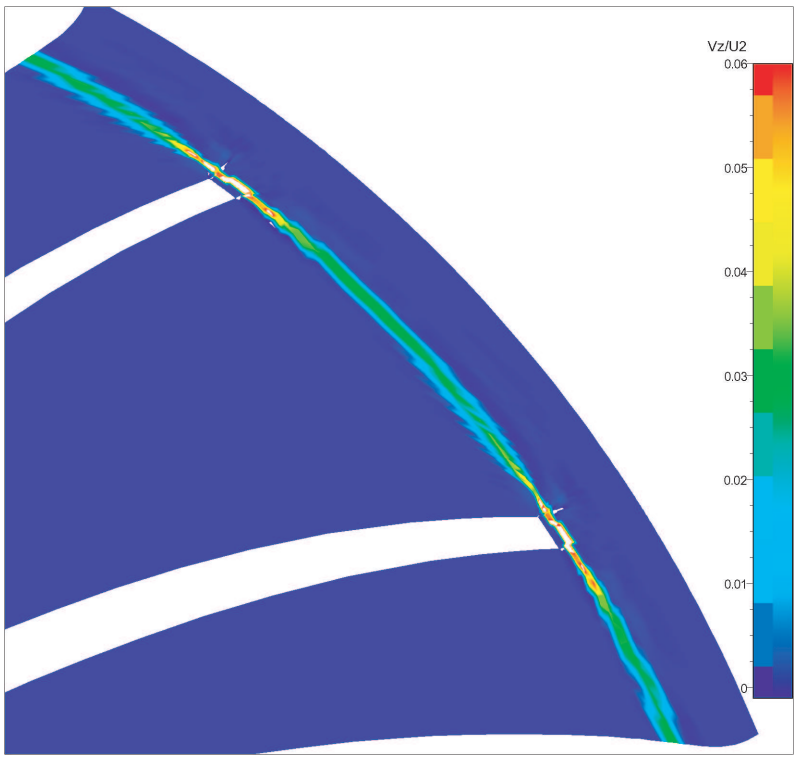

2-5.2: Contour of axial velocity on simulated impeller hub surface, illustrating the axial velocity through the simulated bleed slot.

Figure 2-5: View of leakage flow mesh set-up (top) and resultant velocity through bleed slot (bottom).

out on a dual-processor machine, and took approximately 1500 iterations to converge at near-stall, which amounted to approximately 6 hours of CPU time per operating point when using the fine mesh.

The exit pressure, or backpressure, was raised from one calculation to the next, in this manner, until a steady equilibrium solution could no longer be attained on the finest grid with a reasonable amount of CPU time. The lowest mass flow operating point with a converged, steady equilibrium solution was determined to be the stall point. The stall point determined in the steady calculations occurred at a higher mass flow than what was determined in experiment. The unsteady diffuser-only RANS calculations discussed in Chapter 3 were able to simulate the flow field in the diffuser to a lower mass flow. The diffuser calculations use the flow features at impeller exit from the stage calculations as inlet conditions, so all diffuser calculations with mass flows below the stage calculation stall point used the stall point flow features as inlet conditions.

2.3 Compressor Stage and Diffuser Subcomponent Behavior

This section analyzes the overall compressor performance through the stage pressure ratio characteristic and diffuser subcomponent pressure rise characteristics. The analysis is linked to the experimental data and suggests that several key aspects of the experiment with regards to the flow in the vaneless and semi-vaneless space may possibly be missing from the simulations, which motivates the unsteady calculations discussed in Chapter 3.

2.3.1 Overall Compressor Characteristics

The compressor characteristic at 100% speed is shown in figure 2-6, which compares the experimental total pressure ratio data with the calculated stage pressure ratio data. The black circles and red diamonds correspond to the experimental data with-

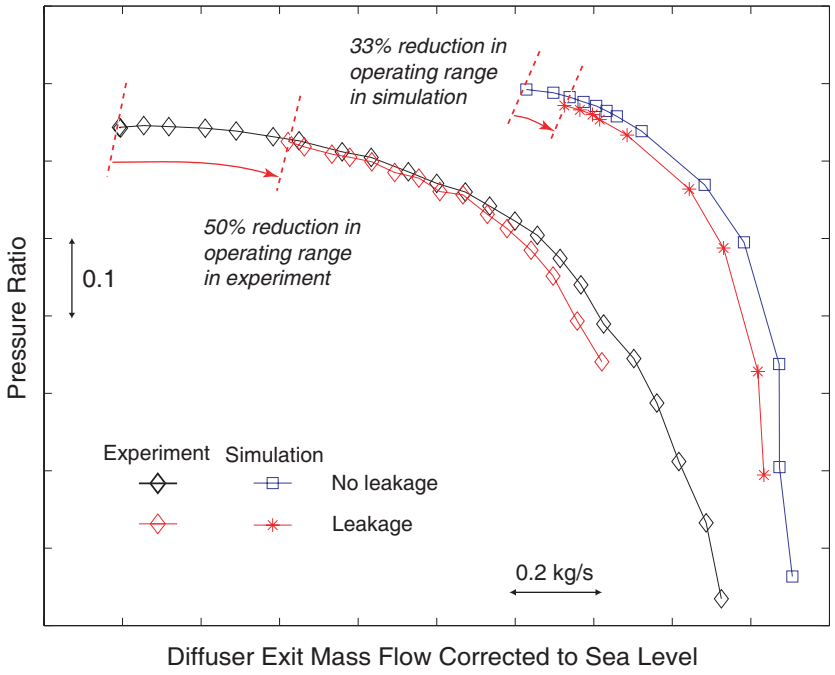

Figure 2-6: Bulk performance of simulated compressor stage at 100% corrected speed.

out and with leakage flow at impeller exit, respectively. The blue squares and red asterisks correspond to the simulation results for the same conditions. The leakage flow, as stated earlier, amounts to approximately 0.5% of the inlet mass flow.

The results of the simulation agree with the experimental data, shown in Figure 1-2, in that the pressure ratio is unaltered with leakage flow. The stable flow range was reduced by approximately 33% in comparison to the 50% reduction due to leakage flow reported in [20], and both simulation characteristics indicate a higher pressure rise and higher maximum mass flow at choke than observed in experiment. In addition, the calculations yield an approximately 50% reduction in operating range when compared with experimental results.

The difference in pressure ratio between experiment and simulation can possibly be attributed to the difference in compressor configuration. As illustrated in Figure 1-1, the test configuration used in the experiments included a volute. The measured total pressure ratio is based on the exit total pressure at the volute outlet. However, the volute, as shown in Figure 2-2, was not simulated which might give rise to reduced stagnation pressure loss in the simulated stage. In addition, the "pinch" used in

the simulated hub and shroud endwalls at the diffuser exit was intended to reduce separation and reverse flow. This geometry modification was necessary to procure convergence in the calculations, but the suppression of loss-generating mechanisms in the flow downstream of the diffuser may have improved the performance.

A more consistent comparison of the stage performance between experiment and simulation is shown in Figure 2-7, which plots the total impeller inlet pressure to diffuser static exit pressure ratio as a function of diffuser exit mass flow corrected to sea level total pressure and temperature. In the experiment and the simulations with leakage flow, the mass flow at the impeller inlet is different from the mass flow at the diffuser exit. In both experiment and in simulation the exit static pressure is measured downstream of the diffuser trailing edge, but upstream of the pinch in the computational domain. The static pressure data for this diffuser exit location were not available for the entire flow range in the experiments, so the characteristic for the no-leakage case is extrapolated as shown by the dashed line.

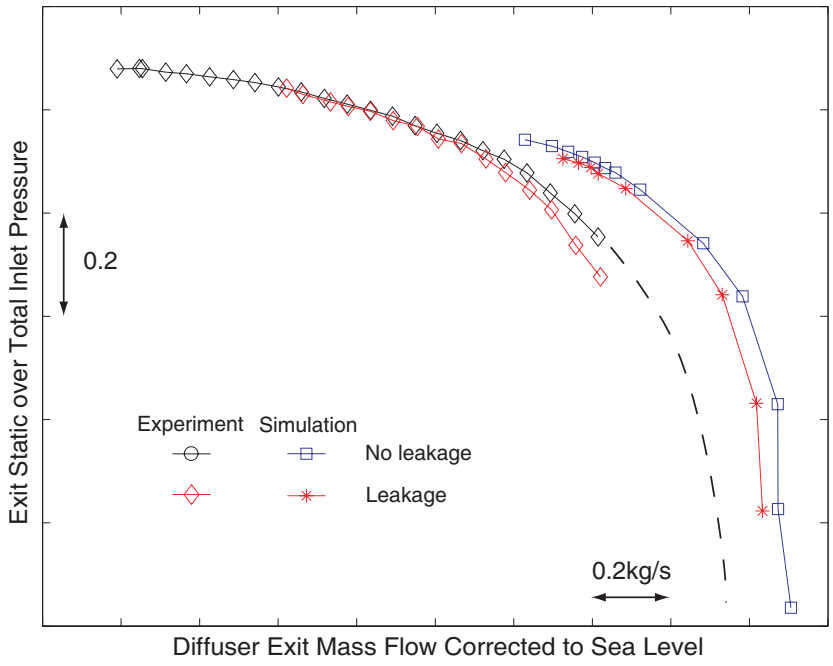

Figure 2-7: Comparison of p_{Tinlet}/p_{exit} between experiments and steady CFD simulations with and without leakage flow at impeller exit.

Figures 2-6 and 2-7 both indicate a difference in exit corrected mass flow between the two simulated speedlines at the choke side of the speedlines. This is a physical

result of extraction of low stagnation pressure endwall flow at the impeller exit and can be resolved by considering the corrected flow at the diffuser inlet. Figure 2-8 plots the total pressure ratio as a function of the corrected flow at the diffuser inlet. Note the difference in scale between Figures 2-8 and 2-6. The difference between

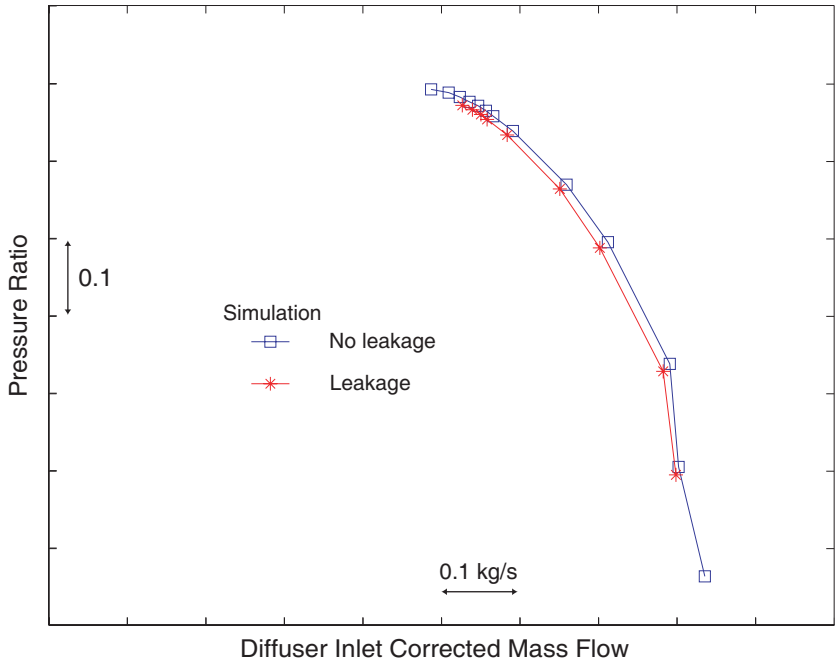

Figure 2-8: Overall performance of compressor stage as a function of diffuser inlet corrected flow.

choke corrected mass flow between the simulations with and without leakage flow at impeller exit is visibly within a reasonable confidence interval.

2.3.2 Diffuser Subcomponent Pressure Rise and Suggested Impact on Compressor Stability

In [20] the static pressure rise in diffuser sub-components was examined to evaluate the dynamic stability of the diffuser with and without leakage flow. The analysis suggests that the reduced blockage resulting from endwall boundary layer extraction redistributes the loading in the diffuser subcomponents. More specifically, the vaneless space diffusion increases, altering and de-stabilizing the flow in the semi-vaneless space.

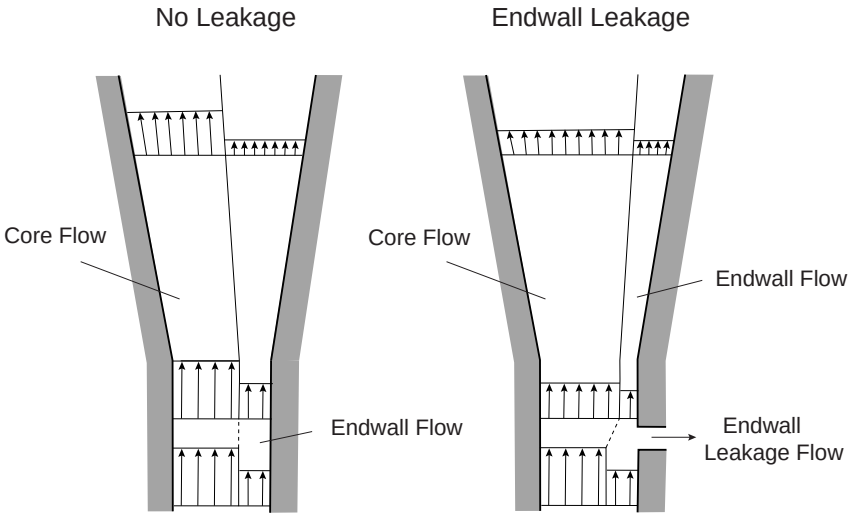

Figure 2-9: Qualitative depiction of change in diffuser static pressure rise due to endwall leakage flow. Figure adopted from [20].

The reasoning behind the change in vaneless space pressure rise due to endwall flow leakage is repeated below from [20]. The results are suggested to be in agreement with the diffuser measurements reported by Reneau et al. [17] and interacting boundary layer calculations in diffusers by Greitzer et al. [7]. The conceptual description is quoted below to elucidate the underlying mechanisms.

> To qualitatively illustrate the effects of endwall boundary layer blockage on diffuser pressure rise, the low velocity region can be modeled as an inviscid deficit flow with a uniform velocity profile. This situation is depicted in Figure 2-9 on the left and can be viewed as the interaction of a viscous flow (the boundary layer giving rise to blockage near the endwall) with an inviscid flow (the core flow in the diffuser generating the pressure rise). The conservation of momentum for steady one-dimensional inviscid flow can be written as
>
> $$\frac{du}{u} = -\frac{dp}{\rho u^2}. \tag{2.5}$$
>
> Together with conservation of mass for incompressible flow along a streamtube
>
> $$\frac{du}{u} = -\frac{dA}{A}, \tag{2.6}$$

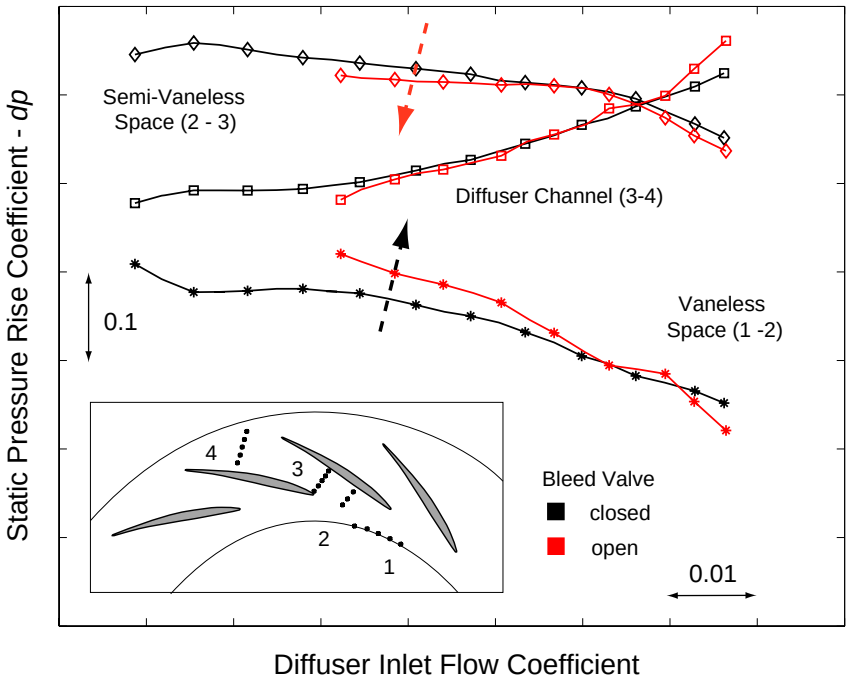

Figure 2-10: Measured static pressure rise of diffuser subcomponents at 100% corrected speed. Figure adopted from [20].

changes in velocity and stream-tube area can be assessed for flow passing through the diffuser. Since stream-tubes near the endwall experience the same pressure gradient dp, the relative deceleration in velocity du/u is greater near the endwall due to the relatively lower velocity magnitude as compared with the core-flow. From continuity the low velocity region grows, decreasing the diffuser pressure rise compared to the situation of uniform flow. With endwall leakage flow, shown on the right in Figure 2-9, the relative deceleration in the endwall stream is reduced increasing the overall diffuser pressure rise. [20].

The above analysis is applied to the redistribution of diffuser subcomponent loading seen in the experiments, shown in figure 2-10. The subcomponent characteristics of a vaned diffuser are a useful metric for analysis of the diffuser stability, as shown by Hunziker and Gyarmathy [10], and by Spakovszky and Roduner [20], whose measurements of the subcomponent characteristics are shown in Figure 2-10 for 100% speed. The vaneless space is the vaneless diffuser between the impeller trailing edge (station

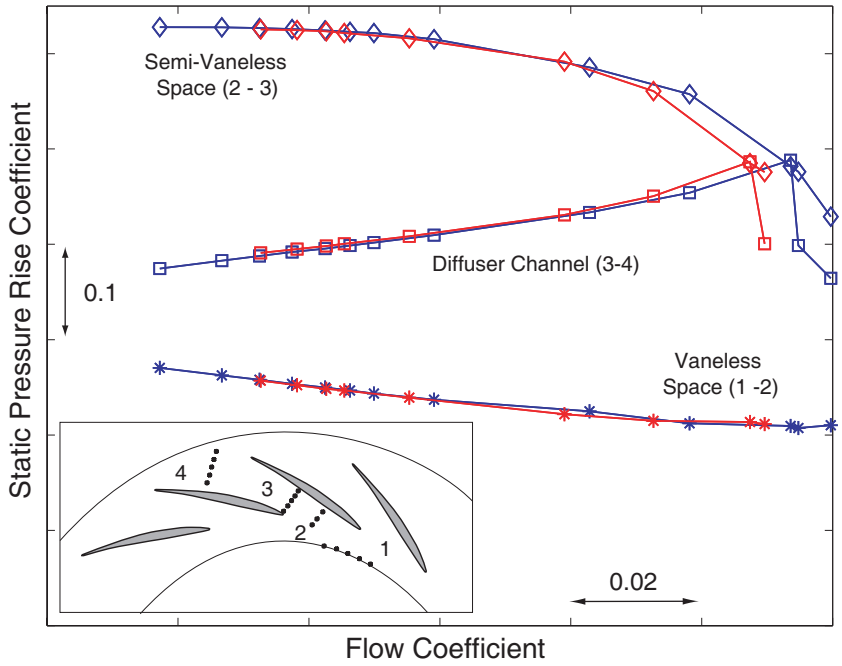

Figure 2-11: Calculated static pressure rise in diffuser subcomponents. The scale shown here occupies approximately the right third of the scale shown in Figure 2-10

1 shown in inset) and the diffuser vane leading edge (station 2). The semi-vaneless space extends from station 2 to the diffuser throat (station 3). Finally, the channel extends from the throat to the diffuser vane trailing edge (station 4).

The static pressure rise in the vaneless space (stars), the semi-vaneless space (diamonds) and the diffuser passage (squares) were determined using area-averaged static pressures on the hub endwall as shown in the bottom-left of the figure. The evaluated pressure rise is expressed as dp in Figure 2-10, and is defined by equation 2.7 below.

$$dp_{A-B} = \frac{p_B - p_A}{\frac{1}{2}\rho_{in}U_2^2} \tag{2.7}$$

The measurements without leakage flow are shown in black, while those with leakage flow are shown in red. The increased diffusion in the vaneless space with leakage flow is suggested to be due to reduced endwall flow blockage as described in detail above. The reduced endwall flow improves the diffusion in the vaneless space as indicated by the black arrow, which reduces the diffusion in the semi-vaneless space, shown by the red arrow.

The same area-averaged static pressure measurements shown in Figure 2-10 were made on the hub endwall of the CFD results and are shown in Figure 2-11. Note that the ranges of mass flow in the experiments and the simulations are different. Figure 2-7 serves as a guide to the relative operating ranges of the data sets. In the simulated results, unlike in the experimental data, the total quantities are known at impeller exit. With the total pressure at impeller exit, the quantity

$$Cp_{A-B} = \frac{p_B - p_A}{p_{T2} - p_2} \tag{2.8}$$

is used in lieu of *dp* in Figure 2-11.

It is noted that in both experimental and the calculated results, the flow coefficient indicated represents the *diffuser* mass flow. For consistency between cases with and without leakage flow, the mass flow used to compute the diffuser flow coefficient is the mass flow exiting the diffuser. Figure 2-11 shows that, in comparison to the experimental results, the changes in component pressure rise due to endwall leakage flow are negligible suggesting that some aspect of the leakage flow or hub endwall flow is not accurately simulated.

Several significant aspects of the experiment with regards to the flow in the vaneless and semi-vaneless space may possibly be missing from the simulations to explain the differences between experiment and simulation. One aspect is the implementation of the leakage flow. In an effort to test the sensitivity of the stage performance to the amount of leakage flow, an additional series of calculations was carried out where the mass flow through the bleed slot was doubled. The change in stage performance due to a doubling of the leakage mass flow was negligible, and suggests that changes due to endwall leakage flow seen in experiment are not caused by the extraction of endwall flow alone, but rather some secondary result of the leakage.

One secondary effect could be related to the annular slot from which the leakage flow is bled, shown in Figure 1-1. This slot, or cavity, may play a significant role due to recirculation in and out of the cavity, similar to results seen in Leishmann and Cumpsty [12]. Leishmann and Cumpsty performed an experimental and computa-

tional study on a bleed slot in a compressor cascade, and identified flow recirculation caused by the blade-to-blade variation in static pressure. The cavity may affect the the endwall blockage differently in cases with and without leakage. The leakage flow can inhibit recirculation which may further modify the flow in the vaneless and semi-vaneless space, leading to the characteristic changes observed in [20]. Additionally, the mixing plane, described in the beginning of this chapter and in this device located in the vaneless space, insulates the impeller exit flow from the unsteady effects due to the upstream influence of the diffuser vanes.

The simulation of endwall leakage flow has not caused changes in the diffuser subcomponent pressure rise characteristics. The reasoning behind the changes in diffuser subcomponent and compressor stage behavior observed in experiment are based on a reduction of endwall blockage. The next section examines the endwall flow field in more detail.

2.4 Hub Endwall Flow Field Details

The analysis performed in [20] suggests that the leakage flow alters the endwall flow by reducing the endwall flow blockage and increasing the loading in the vaneless space. This section will examine the details of the flow field near the hub endwall and attempt to link changes in the endwall flow to diffuser subcomponent performance. The aim is to investigate the mechanisms responsible for the increase in vaneless space diffusion and corresponding decrease in semi-vaneless space diffusion seen in experiment. While these changes were not seen in the simulated result, a close examination of the endwall flow field in the simulation may lend additional insight to the key differences between the experiments and simulations which can be useful in further study.

2.4.1 Endwall Boundary Layer Blockage

First, the hub-endwall boundary layer was calculated in the simulated results to evaluate the effectiveness of the leakage flow implementation and to evaluate the endwall flow features. Pitchwise mass-averaging was performed by the post-processing

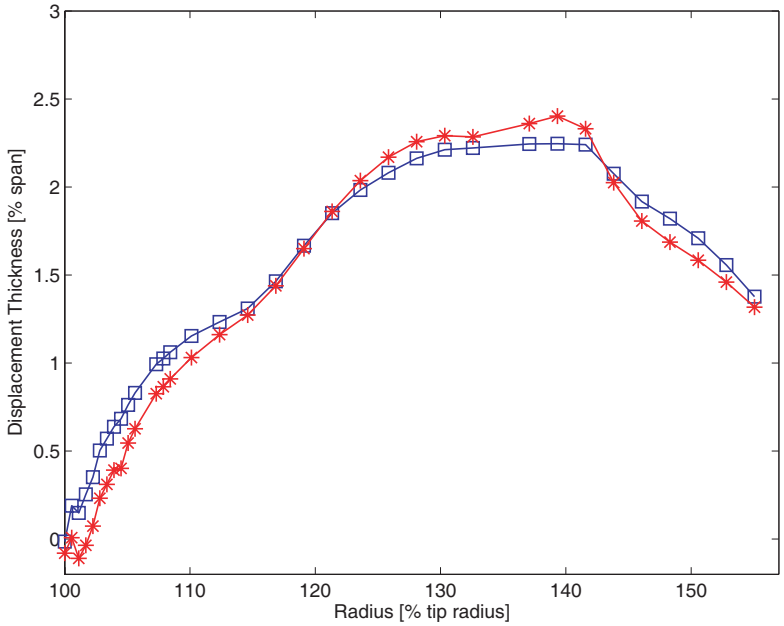

Figure 2-12: Calculated momentum thickness through the diffuser passage, showing a reduction in the hub endwall boundary layer in the vaneless space when leakage flow is bled from the impeller exit.

software, resulting in a meridional representation of the flow through the compressor. The pitchwise-averaged velocity magnitude was determined across the passage span at a range of radii from the impeller exit through the diffuser blade passage, and integrated to determine the displacement thickness, as defined in [7].

$$\delta^* = \int_0^{z_E} (1 - \frac{\rho|V|}{\rho_E|V|_E}) dz \tag{2.9}$$

The reference velocity was assumed to occur at a fixed distance from the endwall of approximately 10% span. In the case of the swirling flow in the diffuser, the velocity magnitude is used to determine the displacement thickness. Figure 2-12 compares the displacement thickness with (red) and without (blue) leakage flow from the impeller exit to the mixing plane. The endwall leakage is extracted between 100 and 102% of impeller exit radius, as shown in Figure 2-5. The plot shows an approximately 30% reduction in displacement thickness at 105% impeller exit radius when leakage flow is applied. The divergence of the red and blue lines at the far left side of the plot shows that the bleed flow extracts low momentum endwall flow, similar to the

qualitative description in Figure 2-9. The convergence in displacement thickness through the blade passage is suggested to be caused by diffusion of the boundary layer across the span and beyond the 10% location of the reference velocity, leading to an underestimation of the displacement thickness value.

The area ratio in the vaneless space is approximately 1.15, where, according to data presented in [17], a 30% reduction in blockage could result in a 10-20% increase in diffuser pressure rise. In the experiments, the vaneless space diffusion increases approximately 10-15% due to endwall flow leakage, and it is suggested that this is due to reduction of the endwall boundary layer blockage. However, the hub endwall boundary layer only measures the blockage on one side of the passage, so a more appropriate measurement of the blockage is necessary.

The flow blockage, defined in [7] and [2], represents the amount of unused flow area in a passage, and can be written as

$$B = 1 - \frac{(\int \rho v dA)}{(\int (\rho v)_{max} dA)} \tag{2.10}$$

Figure 2-13 shows the blockage B computed in the vaneless space upstream of the mixing plane at a near-stall operating point. There is little difference between the case with and the case without leakage, and the leakage case, shown in red, has a slightly higher blockage quantity at approximately 107% tip radius. In addition, the blockage value decreases through the vaneless space, while the displacement thickness shown in Figure 2-12 increases. This suggests that while the endwall displacement thickness may decrease due to leakage flow in the simulations, the blockage does not appear to be affected significantly enough to effect the change in vaneless space diffusion due to leakage seen in experiment. As discussed above, an increase of the amount of simulated bleed flow also failed to produce the changes in diffuser pressure rise seen in the experiments. This result suggests that the change in blockage in the diffuser passage may be due to and affected by recirculation in the bleed slot cavity, which is not included in these simulations.

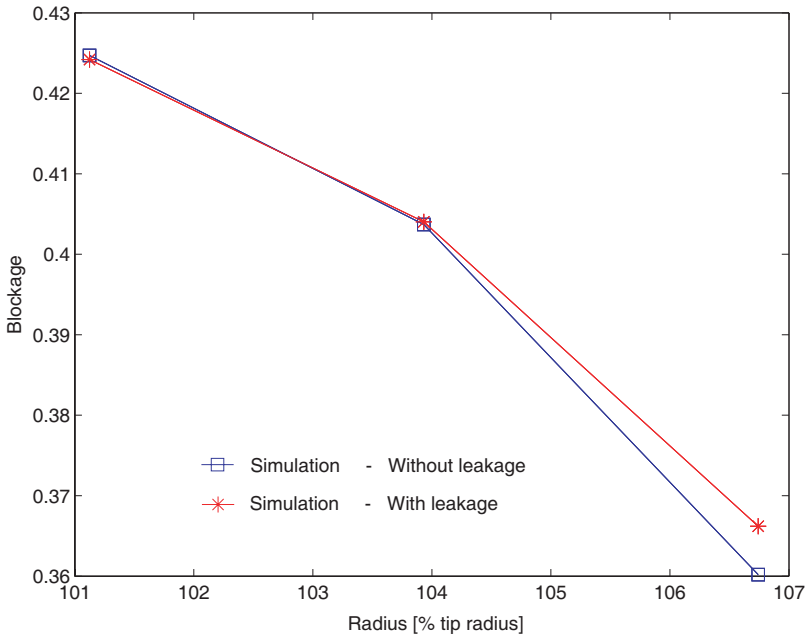

Figure 2-13: Plot of blockage quantity through vaneless space of diffuser between impeller exit (at 100% tip radius) and mixing plane (at 107% tip radius) for an operating point near stall.

2.4.2 Endwall Cross-Flow

The reduction in endwall boundary layer blockage also suggests a reduction in the endwall cross-flow, which can reduce separation in the diffuser passage. This section attempts to qualitatively and quantitatively assess the degree of change in the endwall cross-flow, which may lend further insight on the effects of the leakage flow in the vaned diffuser on the diffuser pressure rise. To illustrate the concept of a boundary layer with cross-flow, a sketch of the endwall region is adopted in Figure 2-14 from [11].

The cross flow in a turning passage can be described with the Squire and Winter [8] expression for the relation between exit streamwise vorticity, ξ, and inlet normal vorticity, η, in terms of the flow turning angle $\Delta\alpha$ and assuming the shear is weak [2] [9].

$$\xi = -2\Delta\alpha \cdot \eta. \tag{2.11}$$

The inset in figure 2-14 is a useful representation of the endwall cross-flow which plots the cross flow component v/U versus the streamwise velocity component u/U. The

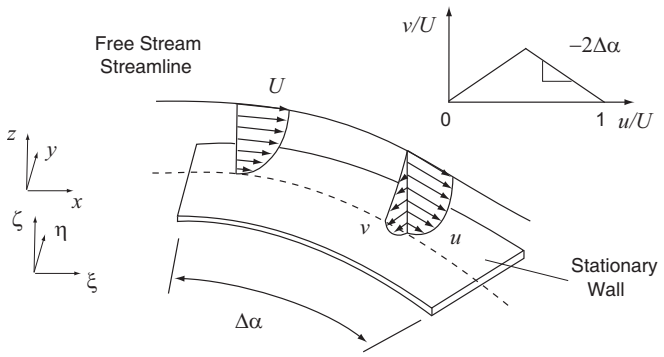

Figure 2-14: Sketch of endwall flow field with inlet normal vorticity. Figure adopted from [11].

inner leg corresponds to the viscous portion of the endwall boundary region, while the outer leg corresponds to the inviscid portion and has a slope equal to the ratio of streamwise vorticity to the inlet normal vorticity. In the case of a stator or vaned diffuser, there is an inlet skew to the boundary layer due to the rotating hub surface and thus a positive streamwise vorticity at the diffuser inlet, so Equation 2.11 can be rewritten as

$$\xi_2 = \xi_1 - 2\Delta\alpha \cdot \eta. \tag{2.12}$$

With the pitchwise-averaged velocity data from the simulations, the polar plot shown in the inset of Figure 2-14 can be plotted for operating points with and without bleed flow, and is shown in Figure 2-15 at two different radial locations in the vaneless space. The red points correspond to a case with leakage flow, and the blue points correspond to a case without leakage flow. Both cases shown have a similar diffuser inlet mass flow for consistency. Figure 2-15 shows the decreased degree of endwall turning due to the leakage flow because of the extraction of the low momentum endwall flow as shown in Figure 2-12, which, in terms of Equation 2.12, reduces η and ξ_1 at the diffuser inlet. In addition, Figure 2-15 shows a decrease in the endwall skew between radial locations at 105% and 115% of the impeller tip radius. The decrease in the endwall skew does not appear to be caused by any turning of the flow through the diffuser because the change in flow angle is small in a radial vaned diffuser when compared with the turning in an axial stator passage. The decrease in endwall skew is instead suggested to be due to viscous diffusion, indicated also by the

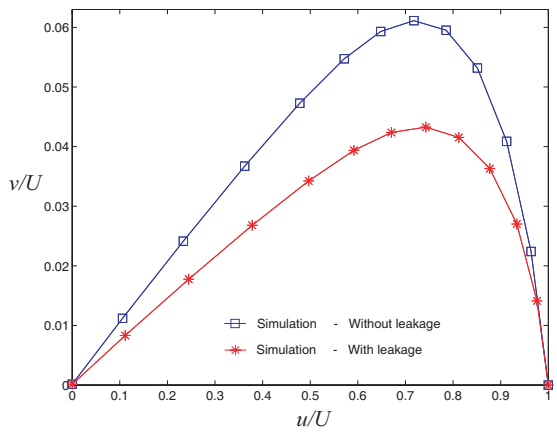

2-15.1: Polar velocity plot at 105% of tip radius

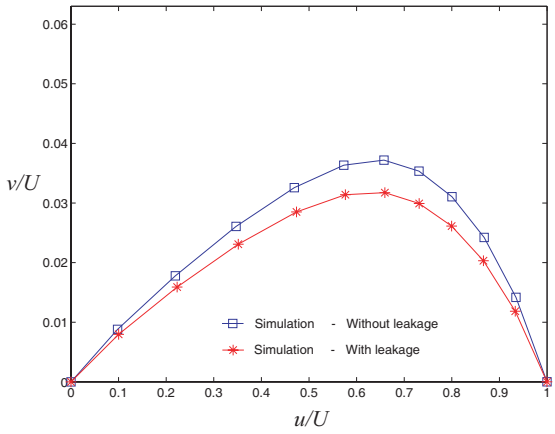

2-15.2: Polar velocity plot at 115% of tip radius

Figure 2-15: Polar velocity plots at two radial locations in the vaneless space. The endwall turning, indicated by the slope of the right-hand side of each plot, is lower in the case with flow leakage, suggesting a lower degree of blockage in the passage due to flow reversal.

fact that the two polar plots at 115% approach the same curve.

Lei et al. [11] used the degree of turning and the incident endwall skew as part of a parameter which reflected the limit of three-dimensional diffusion. The inlet boundary layer skew and cross-flow velocity were shown to contribute directly to accumulation of low momentum fluid near the blade hub-corner, leading to flow separation. Similarly, in the present case the reduced endwall cross flow shown in Figure 2-15 suggests the case without leakage flow is more prone to experience a hub-corner separation.

In the axial stators studied in [11], a hub-corner separation formed on the suction side of the blade due to the strong cross-passage pressure gradient. In the case of a radial vaned diffuser, the radial pressure gradient dominates the cross-passage pressure gradient, and the hub-corner separation grows on the pressure side. To help illustrate the alignment of the pressure gradient in the diffuser passage, Figure 2-16 is repeated below, which shows the contour of the static pressure coefficient through the vaned diffuser passage from the mixing plane to the exit of the diffuser domain. The isolines are at intervals of 0.05 of static pressure coefficient.

The contours of static pressure coefficient in Figure 2-16 indicate a pressure gradient aligned with the streamwise direction through the passage. This suggests that the turning of the swirling endwall flow is towards the pressure side of the diffuser vane.

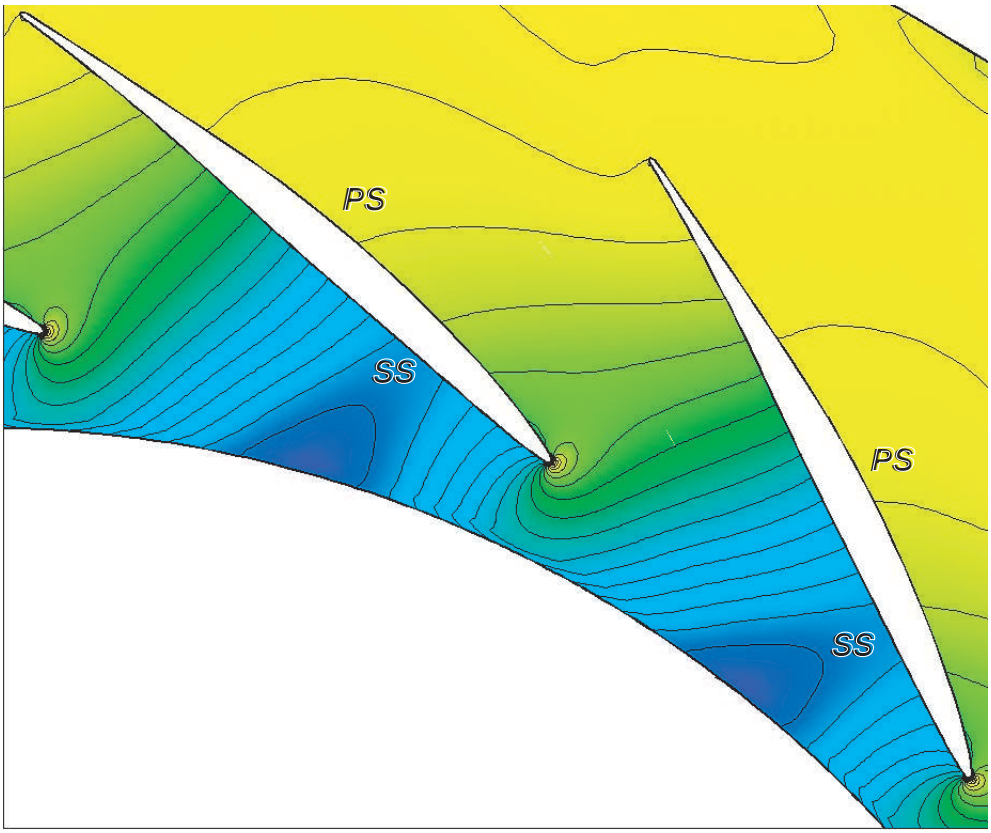

Figure 2-16: Contour of static pressure coefficient (isolines at 0.05 intervals) for an operating point near stall without leakage at impeller exit. The cross-passage pressure gradient is negligible compared with the streamwise pressure gradient in the diffuser passage.

Lower momentum endwall flow is turned inward to a greater extent than the streamwise flow because the lower momentum flow experiences the same pressure gradient as the inviscid core flow and therefore must have a smaller radius of curvature.

Figure 2-17 shows the streamlines in the hub endwall flow (left) and in the mid-span flow (right) in a case without endwall leakage at impeller exit. The streamlines originate at a distance of 0.4% of the diffuser span from the hub endwall in the case on the left. The two figures illustrate the smaller radius of curvature in the hub endwall flow versus the mid-passage flow, following the above discussion. Additionally, the hub-corner separation can be seen as an accumulation of streamlines on the pressure side of the diffuser vane at the hub endwall.

The hub-corner separation is more easily viewed in Figure 2-18 which shows contours of the radial velocity component $V_r/|V|$ for a case without leakage (top) and with leakage (bottom) at similar diffuser inlet corrected flow. Only values from -1.0 to +0.1 of $V_r/|V|$ are shown to highlight regions of reverse flow. The view is from the direction of the shroud at the domain outlet.

When leakage flow is applied the hub-corner separation is drastically reduced to the point that it is not visible in Figure 2-18, suggesting that the differences shown above in displacement thickness and endwall flow turning caused by leakage flow are sufficient to have an effect on flow blockage in the diffuser passage. As noted above, the hub-corner separation is on the pressure side of the diffuser vane rather than on the suction side as in the axial stators studied in [11].

The presence of a hub-corner separation is suggested to play a role in the dynamic stability of the diffuser as a whole, or in its individual subcomponents. Throughout the operating range of the diffuser, the channel downstream of the throat is dynamically unstable as shown by its positive slope in Figure 2-11. The impact of the passage blockage caused by the hub-corner separation is to decrease the channel pressure rise even further, but in the simulations, the difference in separation between cases with and without leakage flow shown in Figure 2-18 does not amount to a change in channel pressure rise. It is suggested that simulating the leakage flow without the potential recirculation in the bleed slot cavity is insufficient to demonstrate the performance

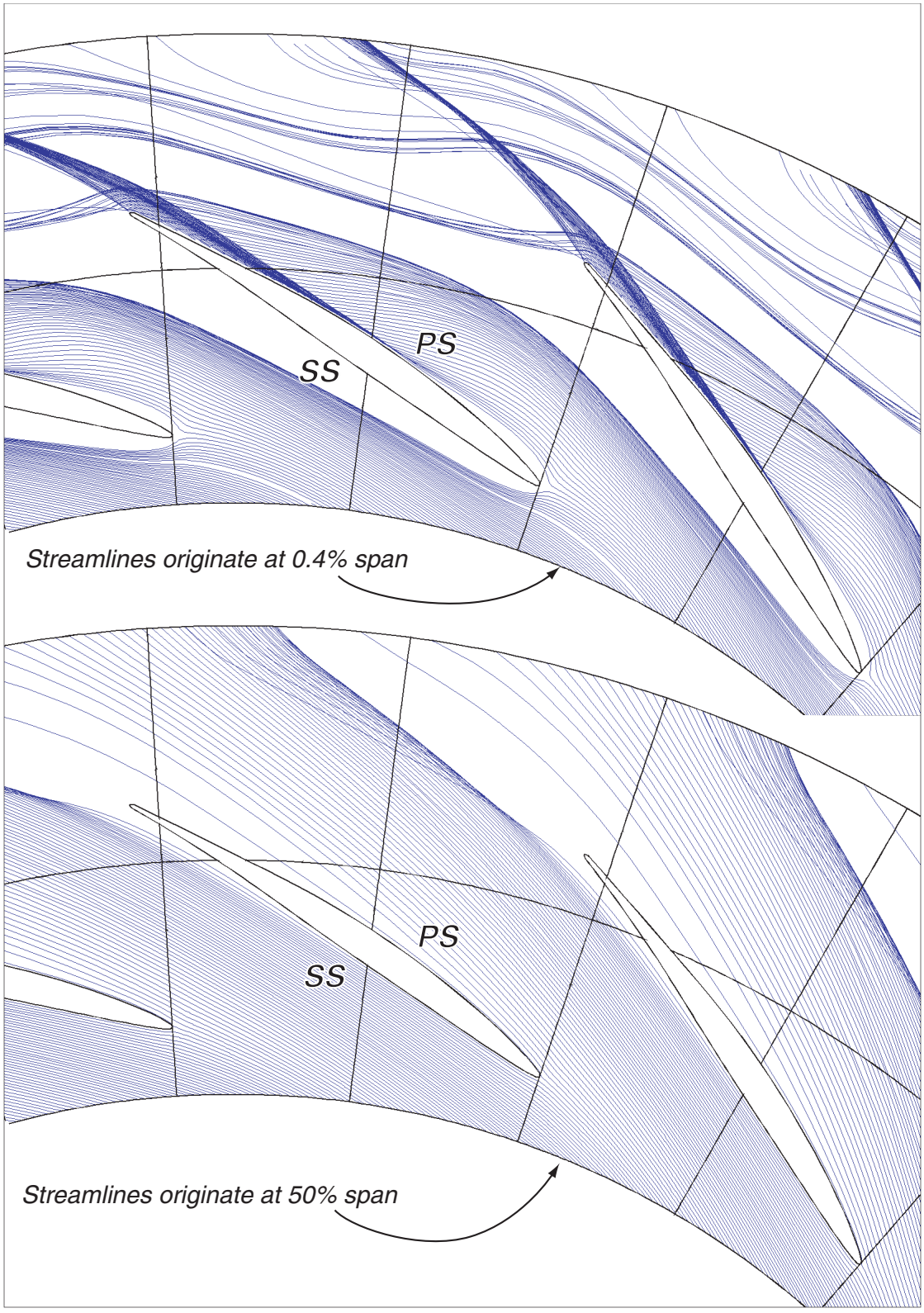

Figure 2-17: Streamlines originating at 0.4% span (top) and 50% span (bottom) from the hub endwall, showing the differences in streamline curvature between boundary layer and core flow in the diffuser passage.

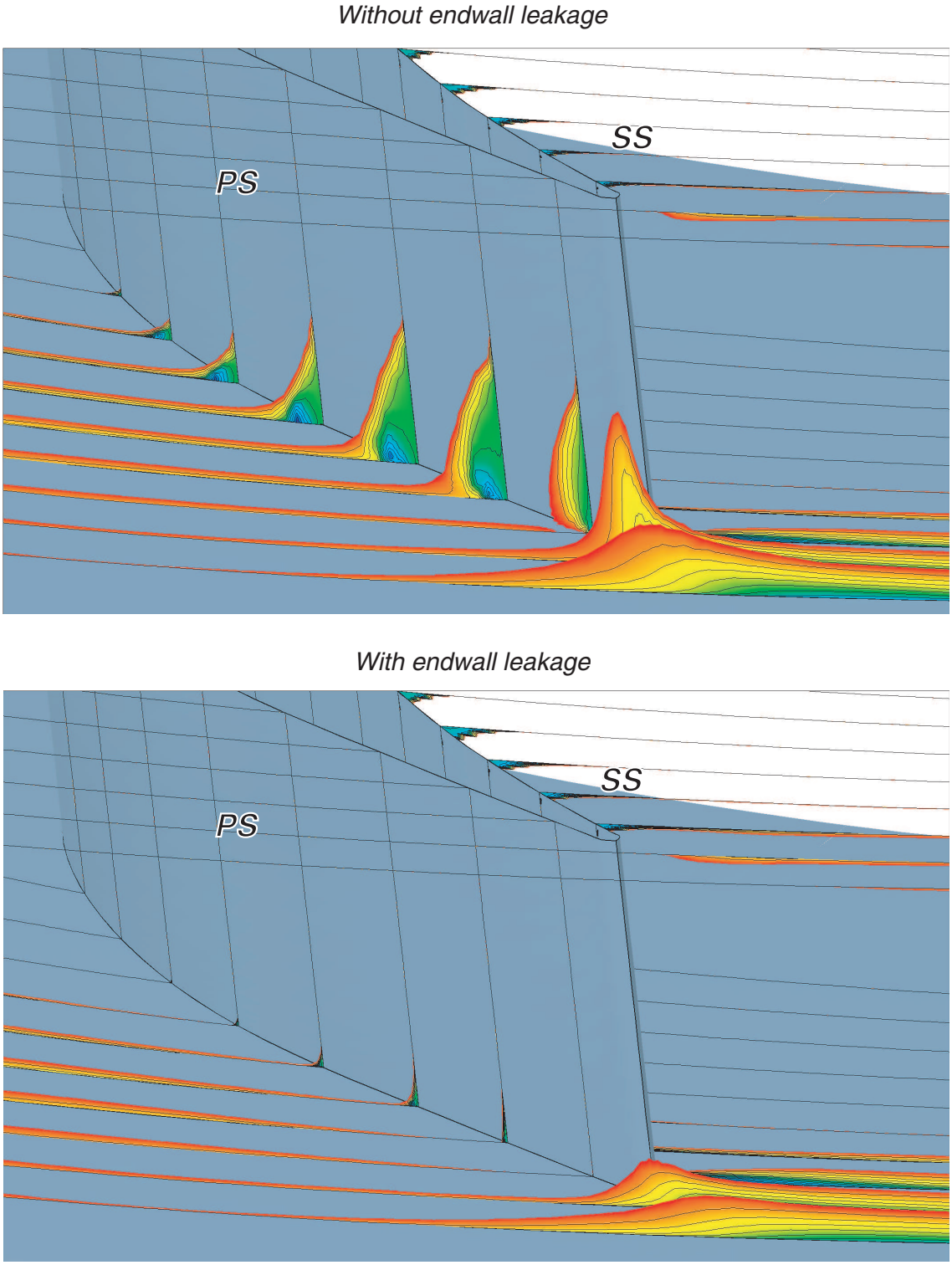

Figure 2-18: View of diffuser vane hub-corner for simulation cases with and without leakage flow at impeller exit. The diffuser inlet corrected flow is similar in the two cases and near the stall point.

changes reported in [20].

2.5 Summary and Conclusions

In this chapter a steady 3D RANS calculation performed on the centrifugal compressor stage at 100% corrected speed was examined. The overall stage performance, diffuser subcomponent static pressure rise, and endwall flow details such as boundary layer thickness, boundary layer turning, and the presence and source of hub-corner separation were addressed to evaluate the effect of leakage flow on bulk performance and flow details. In response to the research questions, the steady-state flow simulations do not fully capture the changes in diffuser subcomponent performance.

This discrepancy is thought to be due to three possible sources:

1. As shown in figure 2-4, it is difficult to simulate near-stall operating points by setting the exit static pressure. This prevented the simulation of low mass-flow operating points, where the sensitivity of the diffuser flow to endwall flow features is greatest. Calculations using an alternative exit boundary condition, such as mass flow, may be capable of simulating the changes in diffuser subcomponent loading.

2. As stated above, the mixing plane is located in the vaneless space, and lies between stations 1-2 shown in Figure 2-10. Several shortcomings outlined above regarding the implementation of a mixing plane suggest that it is too great an approximation to satisfy the research goals of this thesis.

3. The unsteady flow effects experienced by the diffuser vanes are not included in the steady calculation, which could be an additional factor in the stability of the compressor stage. This will be addressed in Chapter 3.

4. The cavity between the hub endwall and the labyrinth seal in the actual compressor is not simulated in the RANS calculation. This cavity may play a role in the behavior of the vaneless space near stall through unsteady flow fluctuations and recirculation through the bleed slot. Ongoing computational work

will address this aspect of the geometry to ascertain its effect on the diffuser flow and compressor stability.

Items 2 and 3 above suggest an unsteady calculation can resolve the discrepancies observed in a steady calculation. However, an unsteady stage calculation presents several issues:

- The inability of a single-passage calculation to model disturbances that encompass multiple blade passages without manifold increases in computational load.
- The difficulties of a sliding-mesh calculation, requiring either a distortion of the geometry (domain scaling), or increased computational and post-processing complexity (phase-lag).
- The large computational expense of a high-fidelity unsteady calculation capable of modeling rotating stall and modal stall waves.

These issues require a trade-off between fidelity of the model and computational time such that an unsteady calculation will be carried out on four passages of the vaneless space and vaned diffuser only. This is discussed in detail in the next chapter.

Chapter 3

Unsteady Simulation of Rotating Flow Disturbances

As discussed in the previous chapter, the steady stage calculations were not able to capture the changes in diffuser sub-component performance and stability when leakage flow at impeller exit is present. The results in Chapter 2 and previous studies suggest that a mixing plane approach [16] and steady calculations do not capture the key flow mechanisms responsible for stall inception in the radial vaned diffuser considered here.

This chapter describes four-passage time-accurate CFD simulations of a vaned diffuser without an impeller. Based on experimental evidence, short-wavelength stall precursors, or spikes, are formed by the diffuser vanes, shown in Figure 1-3. Thus, the simplest configuration to investigate this behavior is to consider the unsteady flow through a vaned diffuser blade row. As hypothesized, the flow non-uniformity exiting the impeller is deemed to influence the unsteady flow in the diffuser, so the simulations use the circumferentially-averaged impeller exit flow field obtained from the steady compressor stage simulation as inlet conditions to setup the swirling flow in the isolated diffuser calculations. This eliminates the impeller from the unsteady simulation, significantly reducing the computational time. At several operating points near to the stability limit of the diffuser row, a spike-like disturbance in total pressure is impulsively applied to the inlet condition to perturb the steady-state flow and to

investigate the formation of stall precursors. The unsteady response of the diffuser flow field to this forcing input is then analyzed using simulated unsteady pressure transducers and is related to the flow stability in the vaneless space.

Several assumptions are made in the investigation described in this chapter which address the elimination of the impeller from the simulation. The first is to ignore the circumferential non-uniformity of the flow exiting the impeller. Previous work [3] demonstrated the importance of the axial non-uniformity over the circumferential non-uniformity of the flow. As such, the pitchwise-averaged impeller exit states are extracted from the steady stage calculations described in Chapter 2 to accomplish this.

The forced perturbation to the inlet flow field is observed to induce flow disturbances that rotate around the circumference in the vaneless space. A forward-traveling spike-like disturbance rotating at 66% impeller speed is found to propagate after the forcing input. Additionally a backward-traveling wave-like disturbance rotating at 43% impeller speed propagates for several rotations, but further work is needed to ascertain its origin. These observations amount to a first simulation of short-wavelength flow disturbances in a radial vaned diffuser. Additionally, an increase in the magnitude of the unsteady static pressure response is observed as the exit static pressure is increased. This is in agreement with expected dynamic behavior as the damping in the vaneless space decreases with mass flow.

3.1 Description of Numerical Simulation

This section describes the detailed characteristics of the numerical simulations. The choice of grid density and the implementation of inlet conditions are discussed in detail.

The computational domain consists of four of the 16 diffuser vanes in the compressor stage studied in [20] and in Chapter 2 of this thesis. While the impeller is not included in these calculations, time is addressed in terms of impeller revolutions. The time step Δt was based on the rotor frequency. Eight time steps per impeller

blade passing were used, yielding 144 time steps per impeller revolution.

Several steady calculations were carried out to initialize the near-stall flow field from the more stable operating points away from stall. These were subsequently used in the unsteady calculations near onset of instability.

Each unsteady diffuser-only operating point was initialized in sequence, similar to the technique described in Chapter 2 for the stage calculations. Approximately eight simulated revolutions, or 1152 time steps, were required for the inlet and outlet mass flows to converge to a steady-state value.

3.1.1 Computational Grid

The computational grid was generated with the AutoGrid software in a configuration similar to the grid described in chapter 2. The key difference is the use of four passages, as described above.

The grid density in terms of number of points per blade passage was reduced by a factor of 10 in the diffuser-only calculations compared to the steady calculations described in Chapter 2 to lower the computational time. The steady calculations required approximately 1000 iterations per fine grid operating point to achieve convergence. For a single operating point in the calculations described in this chapter, 8-10 revolutions are required to allow the flow field to settle to a steady-state. This is equivalent to approximately 60,000 iterations given 144 time steps per revolution.

Also, as will be described in more detail later, the calculations encountered significant convergence issues due to the presence of reverse flow at the domain inlet. This was partly alleviated by the use of a coarser mesh at the diffuser inlet, which prevented the large gradients in the radial velocity component from causing divergence of the solution.

In order to simulate the entire vaneless space between the impeller exit and the diffuser vane leading edge, the inlet surface of the diffuser domain was extended from the mixing plane location at approximately 107% of impeller blade radius to 101% of the impeller blade radius. The grid used approximately 25,000 points per passage, which totals 100,000 points for the entire mesh. A view of the mesh in the axial plane

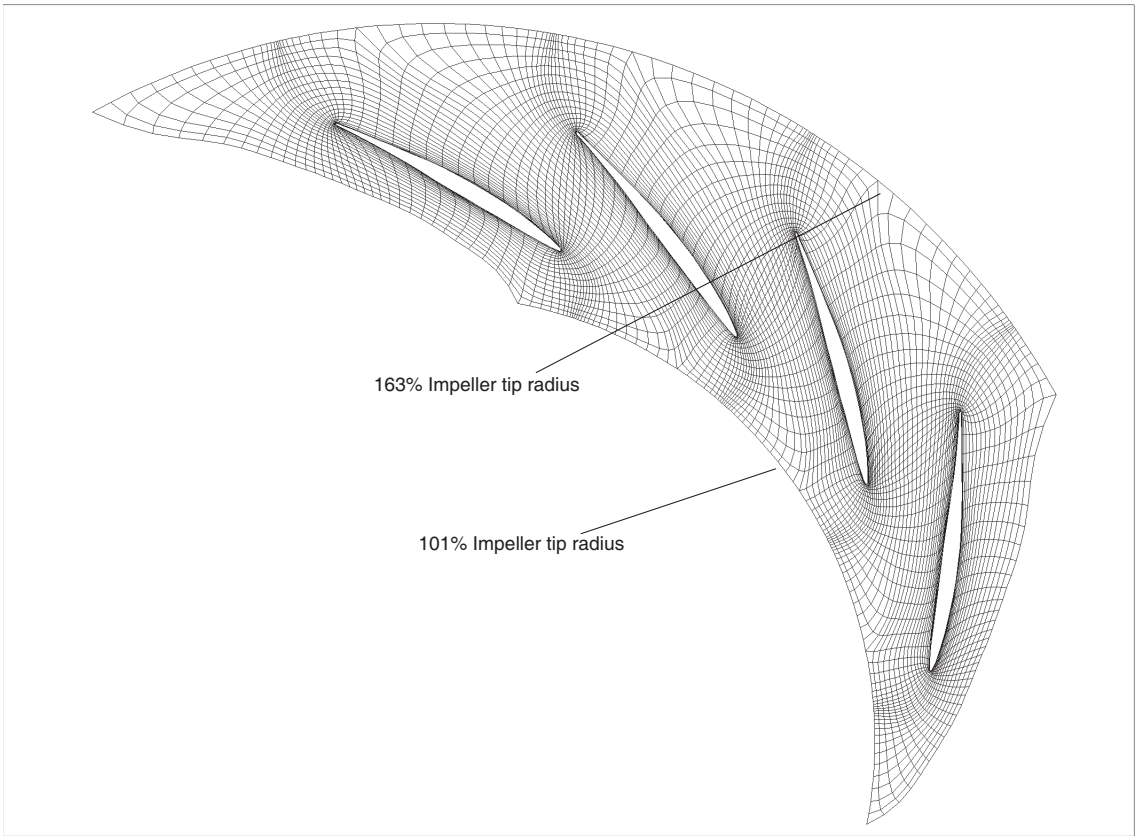

Figure 3-1: Axial view of four-passage diffuser mesh used for unsteady diffuser calculations. Shown in the figure are the radial coordinates of the inlet and outlet boundaries.

is shown in Figure 3-1. The grid in the axial direction is composed of 17 points across the diffuser span.

3.1.2 Inlet Boundary Conditions

One of the objectives of this thesis is to examine the effects of axially non-uniform flow on the performance of a vaned radial diffuser. As discussed by Dawes [3], the circumferential non-uniformity in the flow exiting the impeller is less significant than the axial non-uniformity of the swirling flow. Based on the hypothesis that the non-uniform flow plays a key role in the stability of the diffuser, the inlet conditions were defined as functions of the axial coordinate only. In other words, the imposed inlet flow field was pitchwise-averaged in the circumferential direction, but non-uniform in

the axial coordinate. The flow solver requires total quantities (P_T, T_T) and velocity direction ($\vec{V}/|\vec{V}|$) to specify the inlet flow field. The inlet boundary conditions were obtained from the steady stage calculations without flow leakage at impeller exit as described in Chapter 2.

The pitchwise-averaged flow field described in section 2.4.1 was used to obtain the inlet flow field profiles. The velocity direction was expressed in cylindrical coordinates, corresponding to the cylindrical inlet surface of the diffuser domain. The inlet conditions $V_r/|\vec{V}|$, $V_t/|\vec{V}|$, P_T, and T_T for the near-stall point are shown in Figure 3-2.

Note in Figure 3-2.1 that the radial velocity component is negative at the shroud, indicative of reverse flow at the shroud endwall. The backflow at the computational domain inlet yields an ill-posed problem, resulting in numerical divergence of the solution. To resolve this issue, the radial velocity component at the shroud was limited to a minimum value of $V_r/|\vec{V}| = 0.08$. In addition, the high degree of swirl, indicated by $V_t/|\vec{V}|$ near unity for the entire span, combined with the low stagnation pressure at the shroud surface yielded reversed flow inside the domain near the diffuser inlet. To alleviate this problem the total pressure at the shroud endwall was limited to a minimum value of 0.76 times the design value. It is noted that both of these changes to the inlet conditions amount to a negligible change to the mass-averaged total pressure or to the mass flow at the diffuser inlet. The adjusted inlet conditions for the near-stall point are shown in Figure 3-3.

3.1.3 Outlet Boundary Conditions and Operating Point Definition

Because of the limitations in the use of a mixing plane discussed in Chapter 2, it is challenging to properly match the operating points in the diffuser-only calculations to the inlet conditions obtained from the stage calculations. The inlet and outlet boundary conditions specify total pressure and static pressure, respectively, and the diffuser-only calculations matched the exit static-to-inlet total pressure ratio across

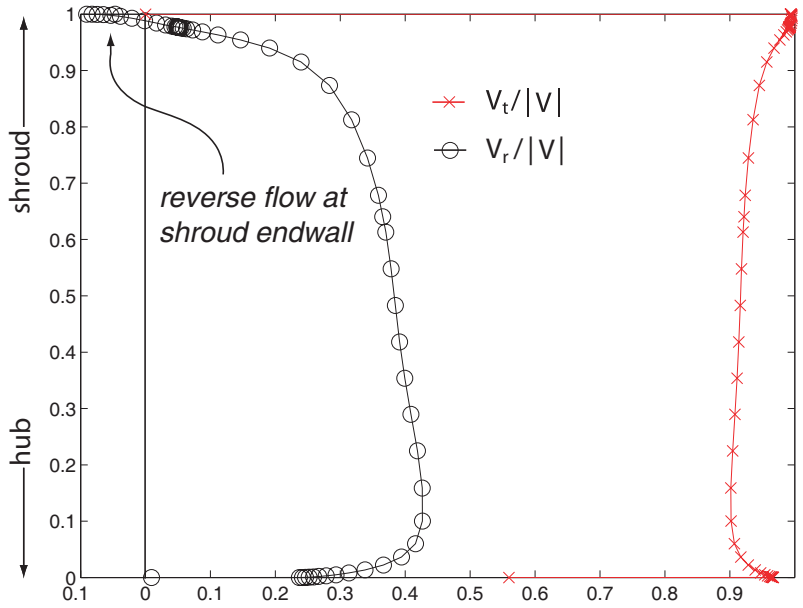

3-2.1: Velocity Direction

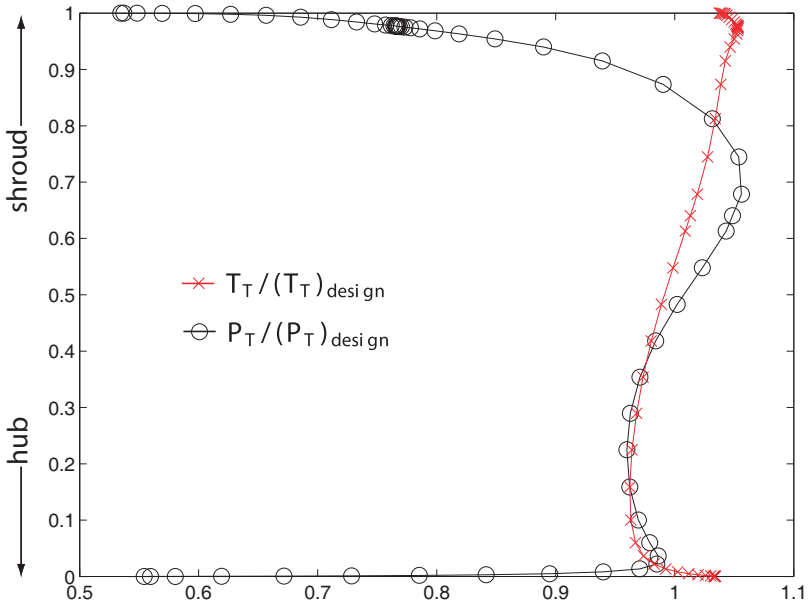

3-2.2: Total Quantities

Figure 3-2: Plots of inlet boundary conditions, illustrating the relative non-uniformity in velocity components and total quantities.

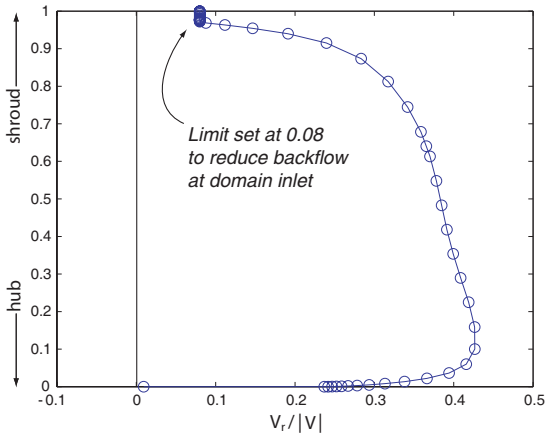

3-3.1: Radial velocity component

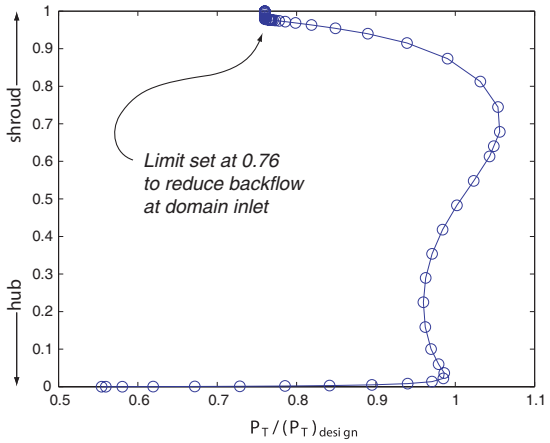

3-3.2: Total pressure

Figure 3-3: Inlet Boundary Conditions

the diffuser to experimental values. Figure 3-4 shows that the stage calculations, shown in blue, had a lower ratio than was observed in experiment. Because of this, the exit pressure, or backpressure, was increased in the diffuser-only calculations, as indicated by the dashed arrows.

The diffuser-only calculations were able to simulate lower mass flows than the stage calculations because the steady stage calculations could not achieve convergence beyond the peak of the compressor characteristic, as discussed in Chapter 2. Because of this, there were no inlet conditions for operating points with mass flows lower than the "stall point" for the stage calculations, shown in Figure 3-5. Given this situation, the inlet boundary conditions were fixed at the the "stall point" and the backpressure was raised to the limit of numerical stability. The unsteady calculations outlined in the discussion therefore do not follow the compressor characteristic as a result of this problem. To resolve this issue, steady calculations beyond the peak of the compressor characteristic are necessary and are a focus of future work.

3.2 Steady-State Results of Diffuser Calculations

Each unsteady operating point obtained as described above was allowed to settle to a steady-state value. These steady-state results of the unsteady simulations along

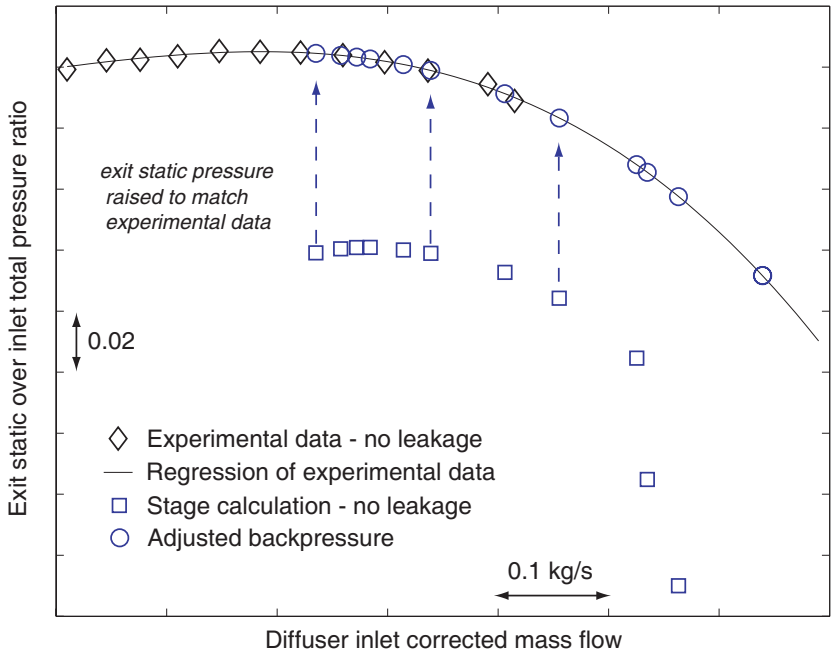

Figure 3-4: Diffuser inlet total to exit static pressure ratio characteristic for experiment, stage simulation, and for boundary conditions used in unsteady diffuser-only calculations.

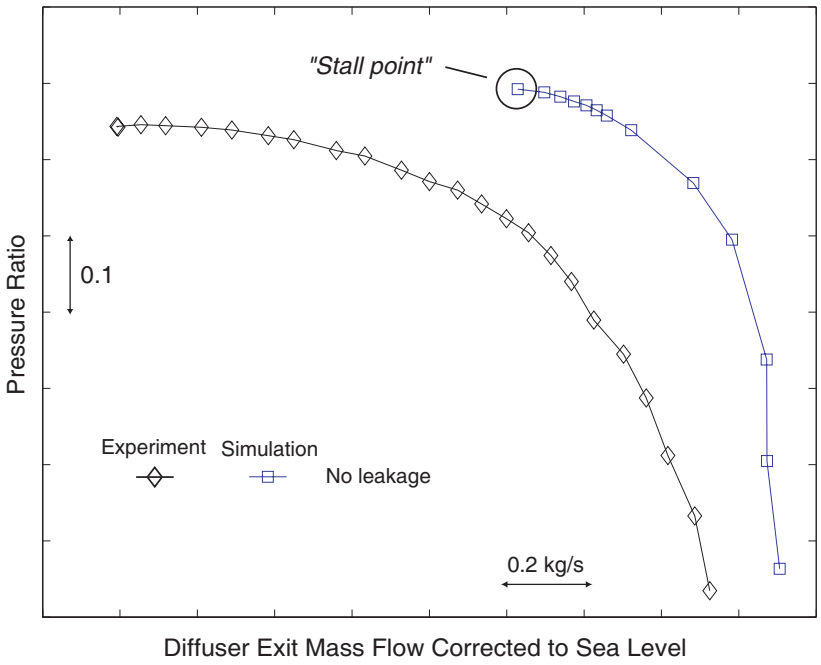

Figure 3-5: Total pressure ratio characteristic for stage calculation and experimental results without leakage flow. Stall point, as defined previously, is circled.

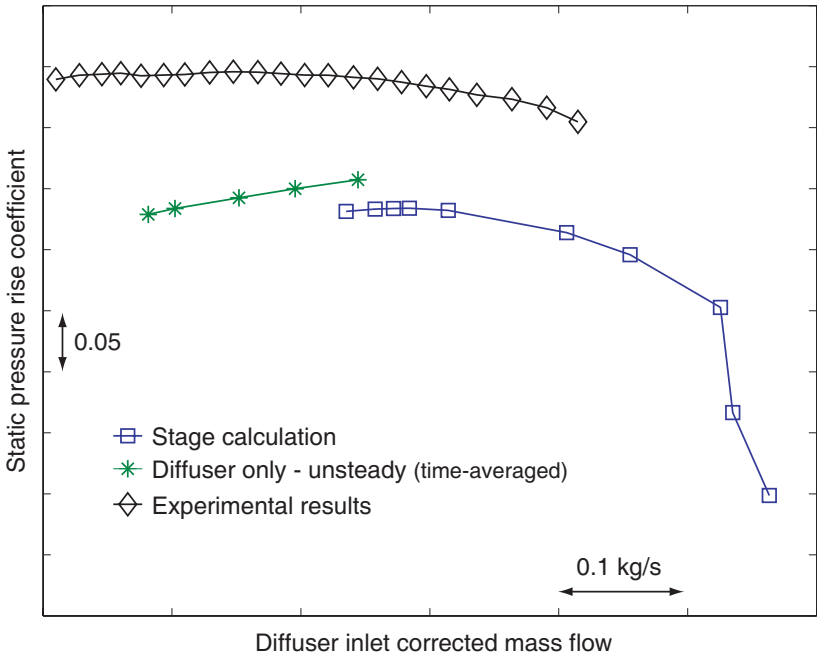

Figure 3-6: Diffuser static pressure rise coefficient calculated from diffuser-only, stage, and experimental data.

with the steady diffuser-only simulations are compared with the experimental data and the steady stage simulations in this section.

3.2.1 Diffuser Component Static Pressure Rise

The static pressure rise coefficient was calculated for the diffuser-only and stage simulations and is compared with the experimental data in Figure 3-6. The plot shows the diffuser-only data in green (stars), the stage data in blue (squares), and the experimental data in black (squares).

The nature of the numerical divergence which limited the diffuser-only calculations was the accumulation of reverse flow near the shroud endwall at the diffuser inlet, which opposed the forward flow imposed by the boundary condition. It is noted that this reverse flow was present in every operating point, but a significant increase in the extent of the reverse flow was observed in the quarter- to half-rotation preceding the termination of the calculation due to divergence.

Figure 3-6 demonstrates that the diffuser-only calculations are capable of simu-

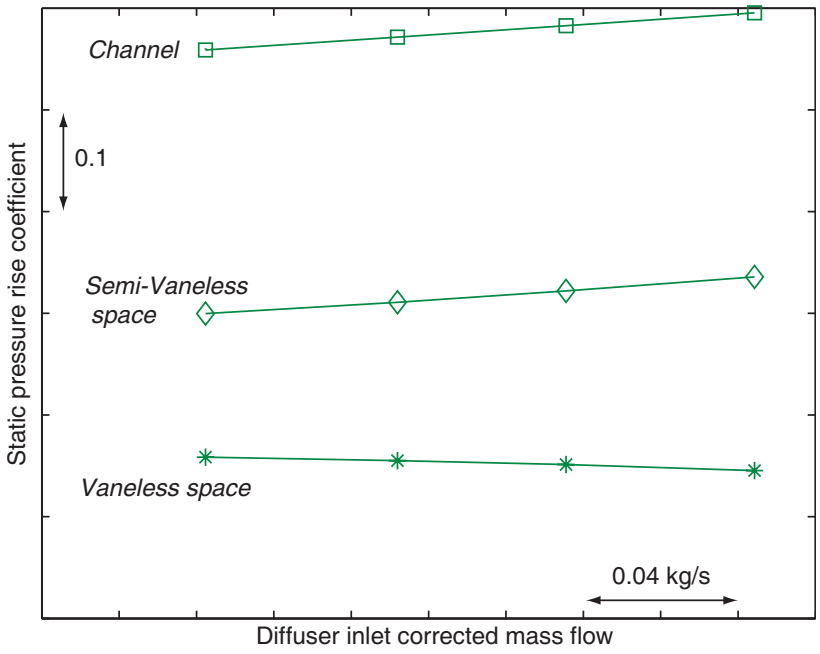

Figure 3-7: Diffuser subcomponent characteristics for time-averaged unsteady diffuser-only calculations.

lating a lower mass flow than in the stage calculations. The minimum mass flow in the stage calculations was approximately 22% higher than the minimum mass flow in the actual compressor experiments, while the minimum mass flow in the diffuser-only calculations was only 6% higher.

3.2.2 Diffuser Subcomponent Pressure Rise and Suggested Impact on Diffuser Stability

An examination of the subcomponent pressure rise can aid in evaluating the ability of the unsteady calculations to simulate the near-stall behavior of the vaneless space and vaned diffuser. Similar to the procedure carried out in Chapter 2, the subcomponent pressure rise data for the time-averaged states from the unsteady diffuser simulations were calculated and are depicted in Figures 3-7.

The slope is positive for the channel (squares) as in the stage simulation, and the semi-vaneless space (diamonds). The vaneless space has a shallow but generally negative slope. The subcomponent pressure rise curves suggest the damping, indicated

by the slope of the static pressure rise data, is nearly zero in the vaneless space and negative in the other components. It is again noted that these curves do not follow the subcomponent characteristics because of the fixed inlet conditions as described above. The data plotted does, however, reflect the behavior of the simulation, and it suggests that the operating points at the left side of the plot are sufficiently near the stability limit to simulate the rotating flow disturbances as outlined in the hypothesis.

3.3 Simulation of Stall Precursors Near Onset of Compressor Instability

Using the converged time-averaged unsteady calculations described above as a starting point, a series of simulations were carried out on the four-passage diffuser domain in order to assess the response of the diffuser flow field to perturbations in the flow exiting the impeller and to investigate the dynamic compressor behavior near the onset of instability. It is hypothesized that the unsteady diffuser-only simulations are capable of capturing the evolution of short-wavelength disturbances in the vaneless space.

The conceptual approach is as follows: Three time-averaged, or steady-state, unsteady operating points closer to stall given a forced short-wavelength perturbation for a short amount of time. The unsteady response of the diffuser to the perturbation is then investigated.

The forced short-wavelength stationary perturbation was imposed near the shroud for a quarter-rotation, or 36 time steps. The forced disturbance was impulsively added to the diffuser inlet condition, and after the 36 time steps it was removed to investigate whether the transient of the forced input further evolves or dies out. The test was carried out on three operating points at the low mass flow limit of the diffuser, shown by points A, B, and C in Figure 3-8. Operating point B has a 0.25kPa higher backpressure than A, and operating point C has a 0.05kPa higher backpressure than B.

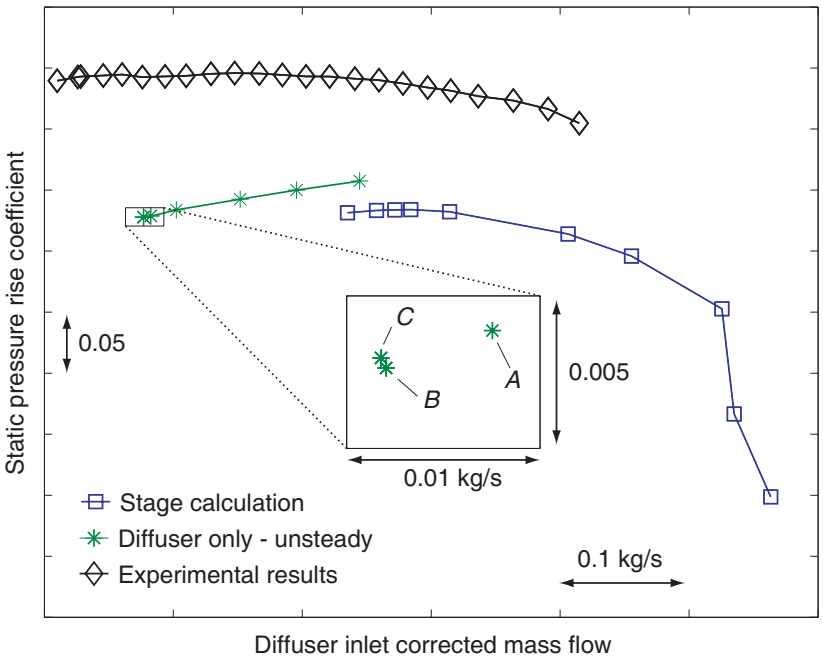

Figure 3-8: Diffuser static pressure rise coefficient. Inset shows operating points A, B, and C used for forced disturbance response.

The short-wavelength forced input had a circumferential extent of 10 degrees and was aligned as indicated in Figure 3-9. Axially, it extended 20% of the passage span from the shroud endwall. Figures 3-10 and 3-11 show the inlet boundary conditions for total pressure used to impose the forced input. The inlet boundary condition function for total pressure defined in Figure 3-3 was extended across the quarter-circumference of the four-passage diffuser domain to produce a pitch-wise averaged boundary condition function. For consistency, this was used to initialize the time steps preceding and following the the forced input.

3.3.1 Time-accurate Evolution of Total Pressure Spike Input

The forced total pressure input disturbance can be observed through a total pressure contour through the local diffuser passage. The disturbance passes through the channel in approximately 50 time steps, or 3/8 of a rotation.

The path of the total pressure forced input is visualized in Figure 3-12 as a percentage of the design value of total pressure at impeller exit. At the top left contour

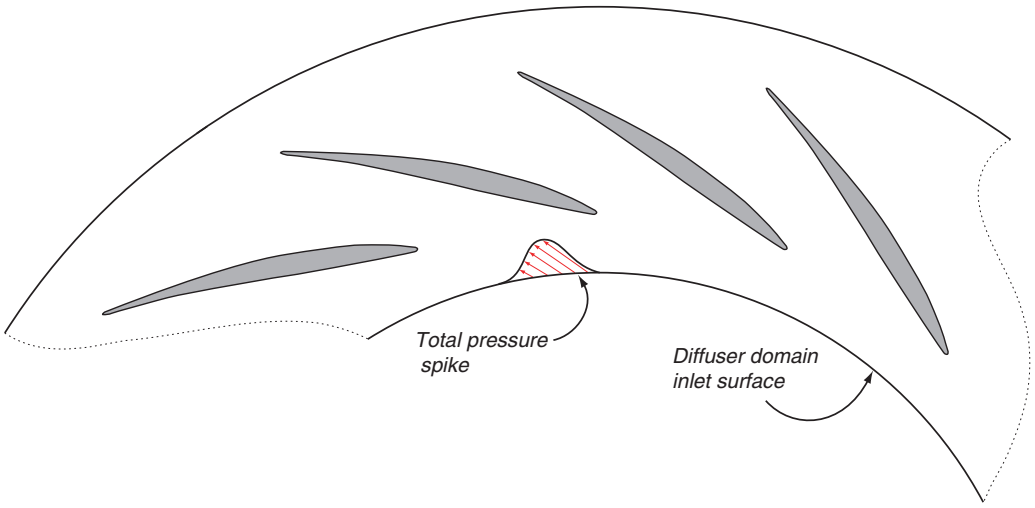

Figure 3-9: Axial view of diffuser showing approximate location of forced perturbation.

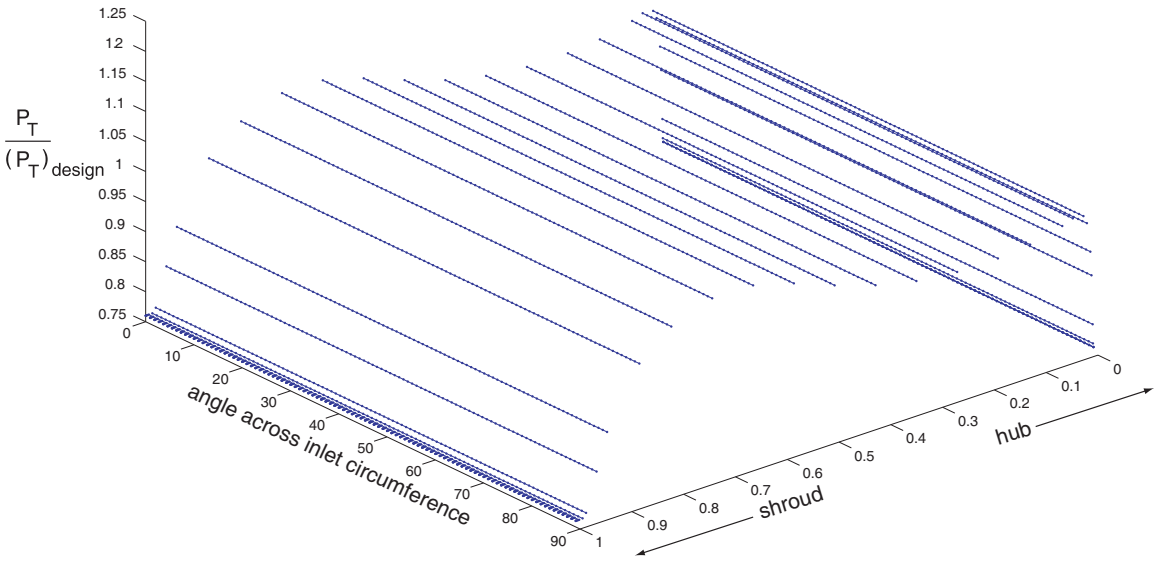

Figure 3-10: Pitchwise-averaged total pressure inlet boundary condition profile projected over the quarter-circumference.

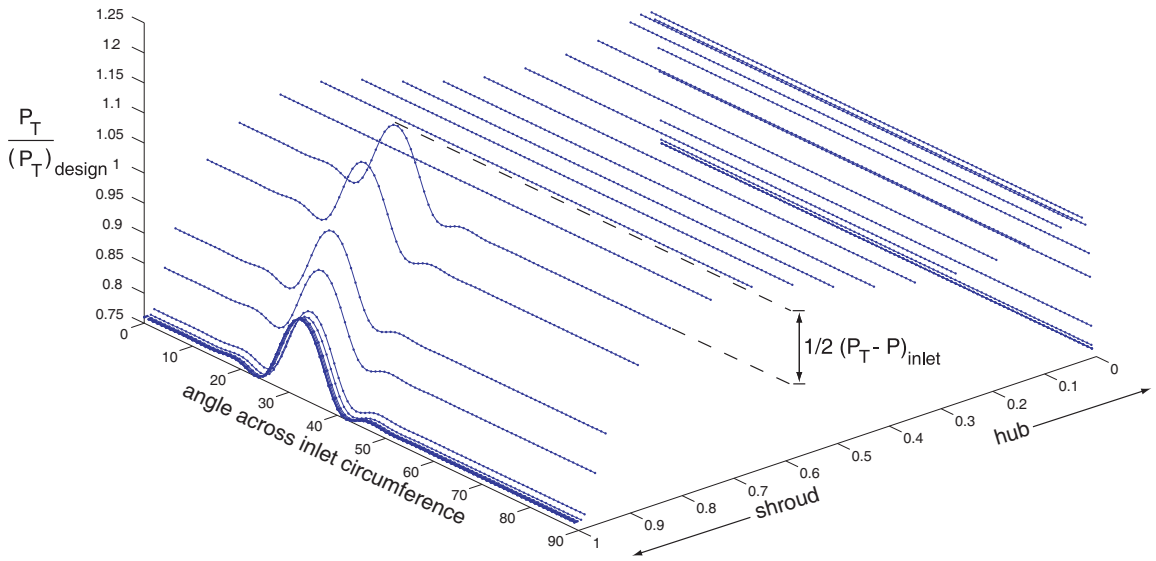

Figure 3-11: Total pressure inlet boundary condition profile from Figure 3-10 with disturbance added.

is the state of the passage before the forced input, at the top right is the passage after the forcing has been applied for 16 time steps, at the bottom left is the passage after the forcing has been applied for 36 time steps, and at the bottom right is the passage 16 time steps after the forcing has been removed from the inlet condition.

The figure illustrates the location and extent of the inlet boundary condition disturbance as it is applied to the diffuser passage. The forced input and the procedure with which it was applied was the same for cases A, B, and C.

3.3.2 Unsteady Static Pressure Response of Spike Input in the Vaneless Space

The responses to the forced input were measured by probing the static pressure around the circumference near the shroud in the vaneless space, similar to the technique used in [3], [19], or [20]. The line of measurement points are shown in Figure 3-13 and simulate unsteady pressure transducers used in experiments.

The values obtained from the measurement points in Figure 3-13 were corrected to determine the unsteady perturbation. The traces of static pressure for the three tests are plotted in Figures 3-14, 3-15, and 3-16 for cases A, B, and C, respectively. The

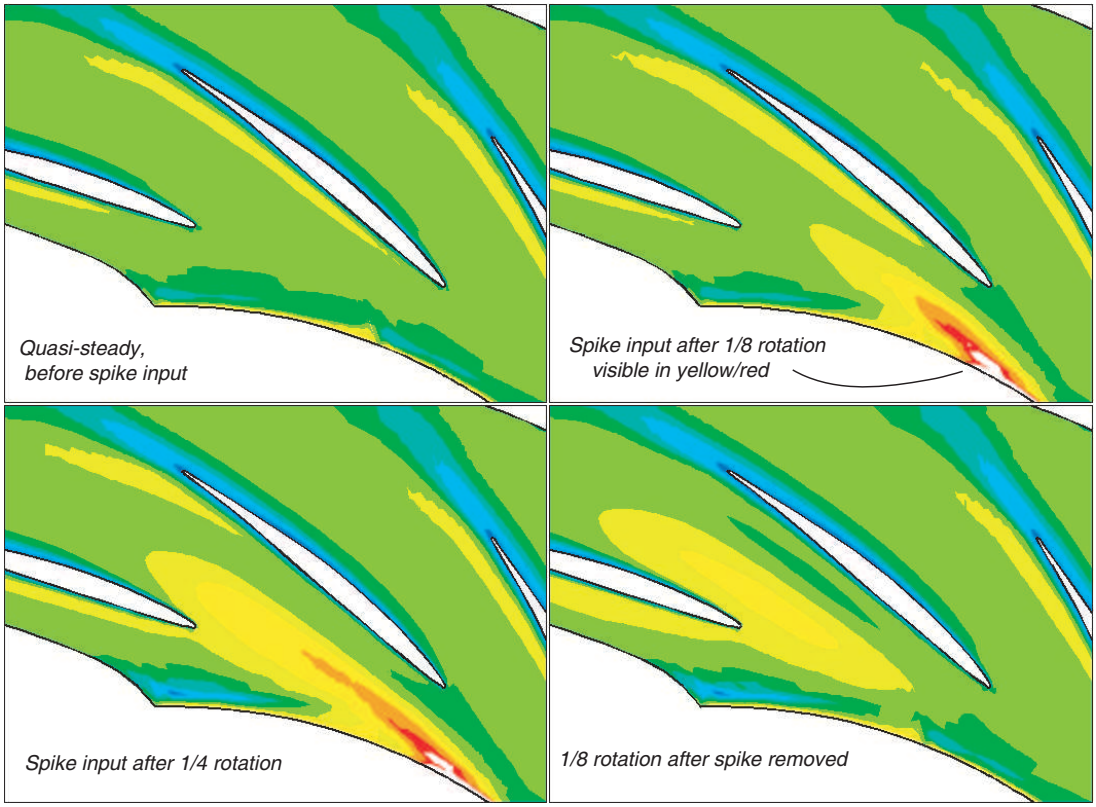

Figure 3-12: Contours of total pressure illustrating the input disturbance as it passes through the diffuser passage.

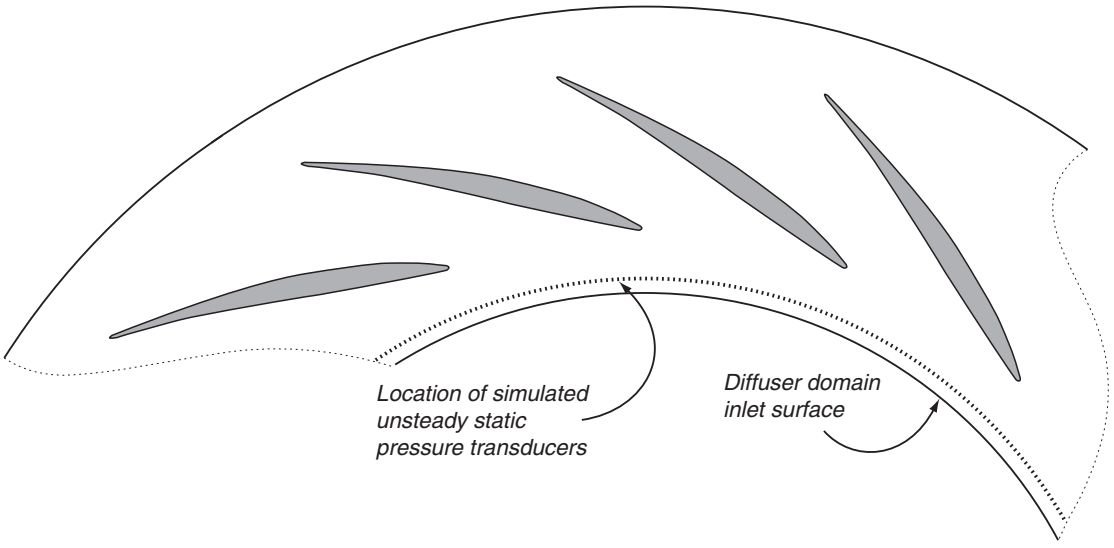

Figure 3-13: Location of a line of simulated unsteady pressure transducers used to examine the effects of the forcing input on the flow in the vaneless space.

traces are plotted to correspond to their locations around the quarter-circumference of the diffuser grid. The horizontal axis indicates time in units of rotor revolutions, starting at two revolutions before the forced input is applied. The direction of impeller rotation is also indicated.

The static pressure traces in Figures 3-14 through 3-16 indicate two short-wavelength disturbances after the forcing is applied, which continue and change over time after it is removed. The first, most visible in cases B and C, originates just after the forced input is removed at 2.25 rotations and at the 90-degree location. This "spike-like" disturbance appears to rotate around the quarter circumference in the direction of the inlet swirl and can be seen to die out in all three cases by approximately 3 rotations. The second, a "wave-like" disturbance, appears at approximately 3 rotations, and can be seen to rotate opposite the direction of the rotor rotation. The backward-traveling wave persists for approximately 1.5 rotations in case B.

The amplitudes of the disturbances increase from case A to case B and from case B to case C. This is indicative of decreased damping in the vaneless space as the backpressure is increased. It does not appear that the damping becomes negative, however, because in all three cases the disturbances appear to diminish. The numerical divergence experienced in case C is a result of numerical problems with increased backflow at the shroud endwall as discussed in Section 3.2.2.

To better discern the rotation rates of the two disturbances, the data obtained for the four-passage diffuser simulation was repeated three times in the circumferential direction to emulate a full-circumference diffuser simulation. This representation is appropriate because it reflects the effects of the spatially-periodic boundary conditions used in the simulations and is displayed in Figure 3-17 for Case B.

Figure 3-17 plots the unsteady pressure trace across the full circumference as described above, with the wave fronts of the forward-traveling waves marked by dashed lines, similar to [20]. The periodic nature of the simulation results in four disturbances traveling around the circumference. In effect, the forcing was applied in four evenly-spaced positions around the circumference, and four identical short-wavelength disturbances formed as a result. Based on the slope of the dashed lines, one wave

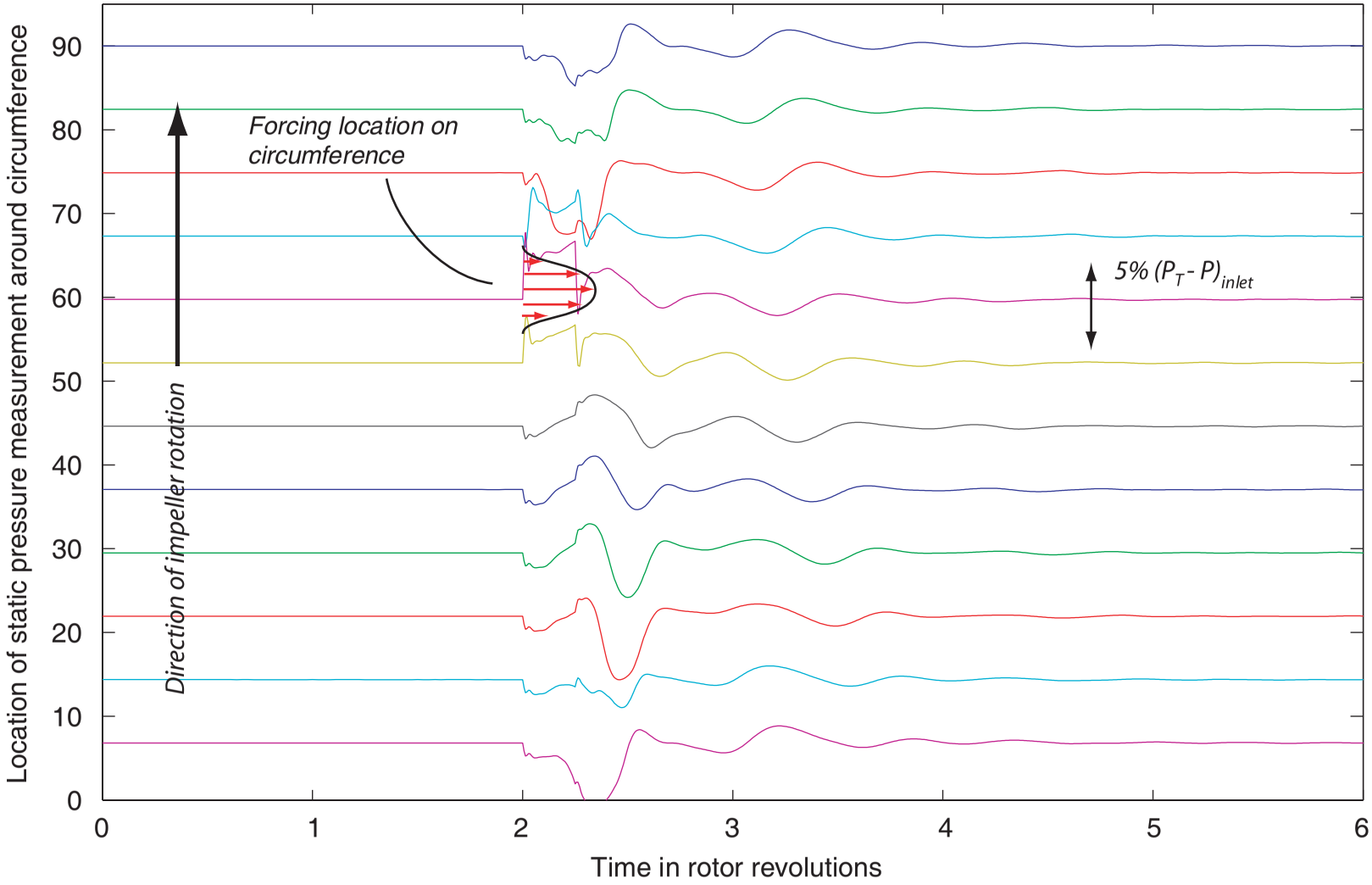

Figure 3-14: Static pressure traces in the vaneless space for unsteady test case A. The forcing is applied at time = 2 rotations for 1/4 rotation. The forcing input is attenuated and the flow returns to its original state.

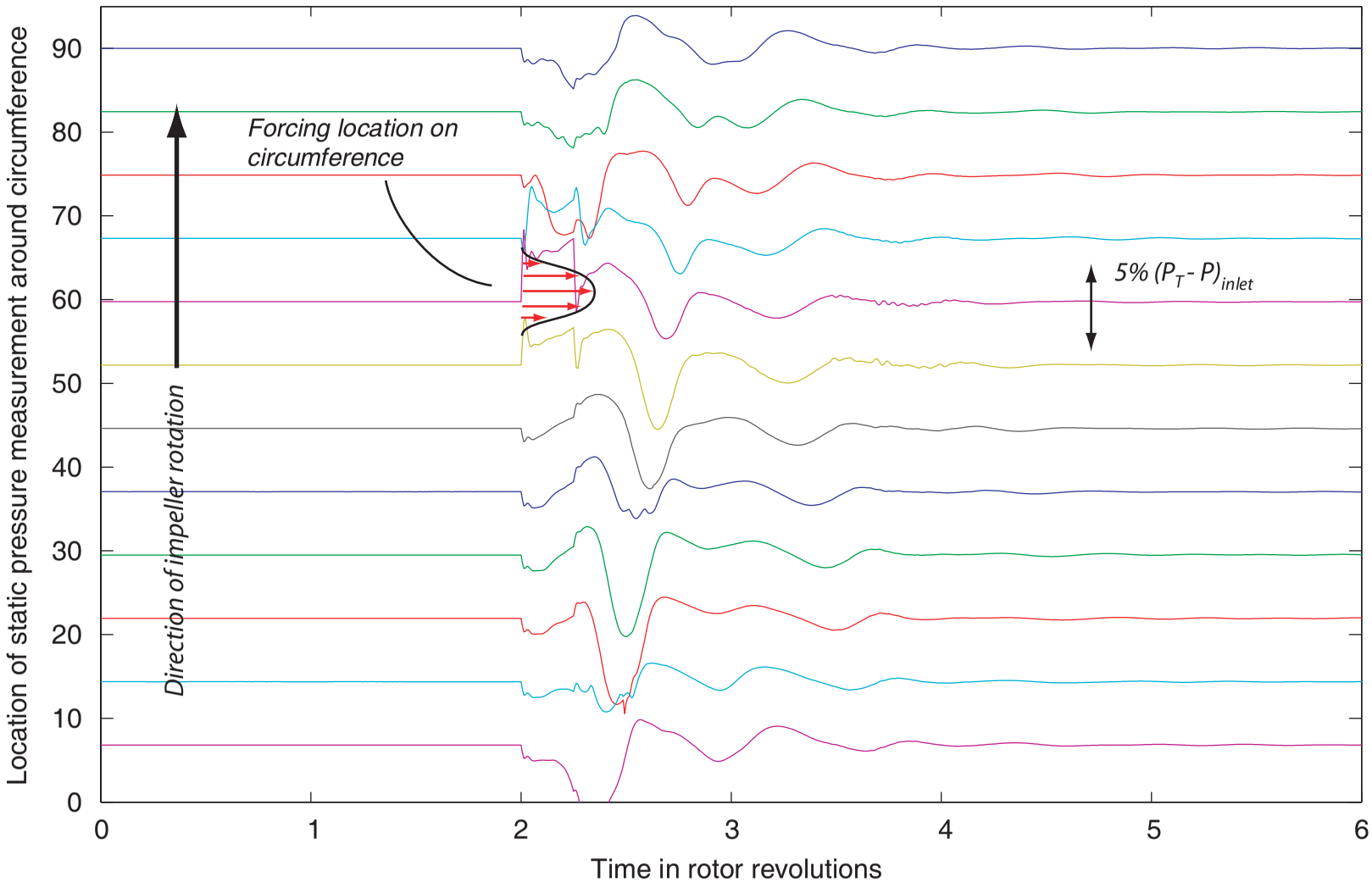

Figure 3-15: Static pressure traces in the vaneless space for unsteady test case B. The forcing is applied in the same manner as in case A. The forcing input is attenuated and the flow returns to its original state, but the magnitude of the response is greater than in case A.

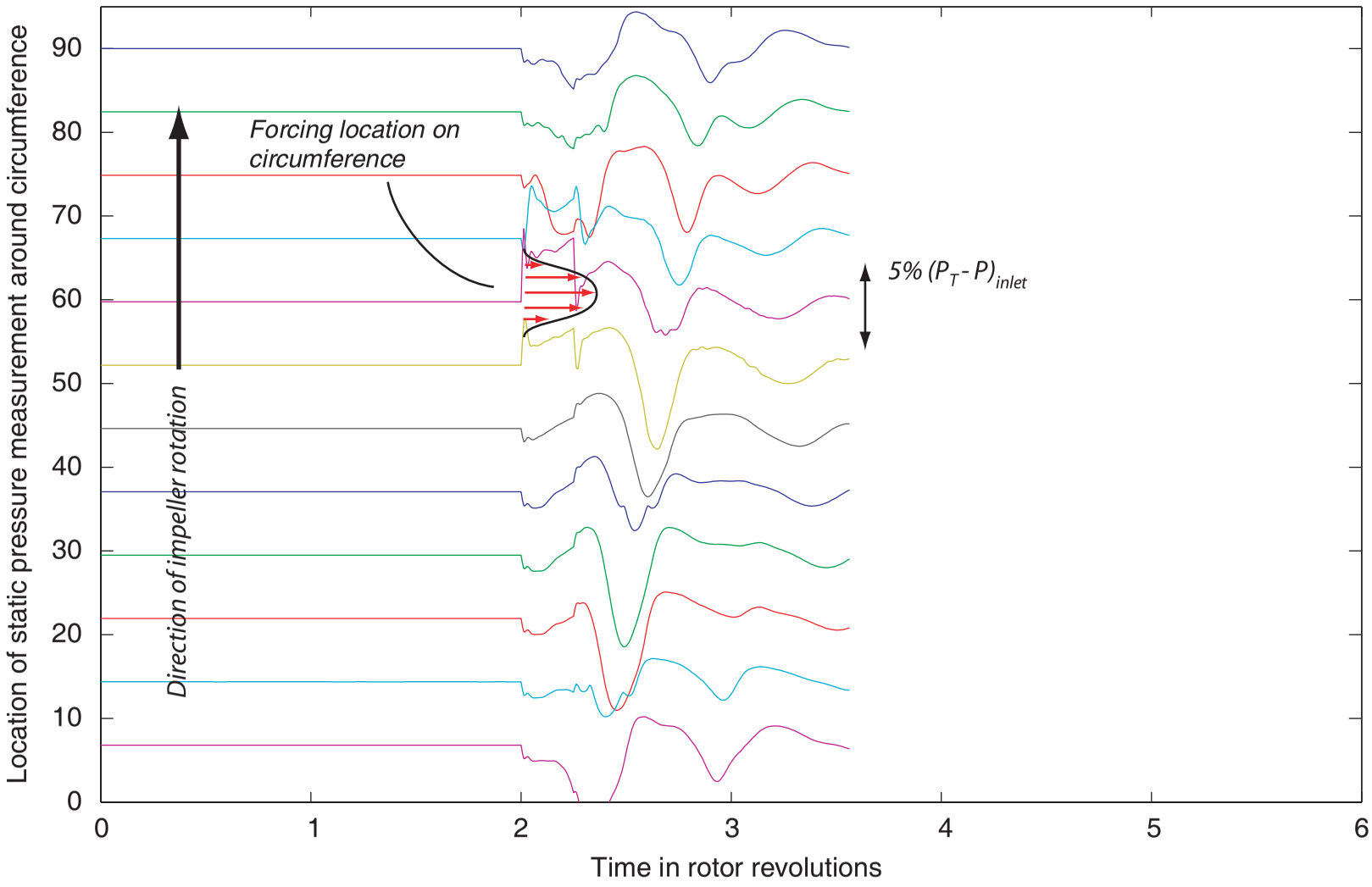

Figure 3-16: Static pressure traces in the vaneless space for unsteady test case C. The forcing is applied in the same manner as in case A. The forcing input appears to be attenuated, but the disturbance in the flow field is sufficient to cause numerical divergence in the simulation.

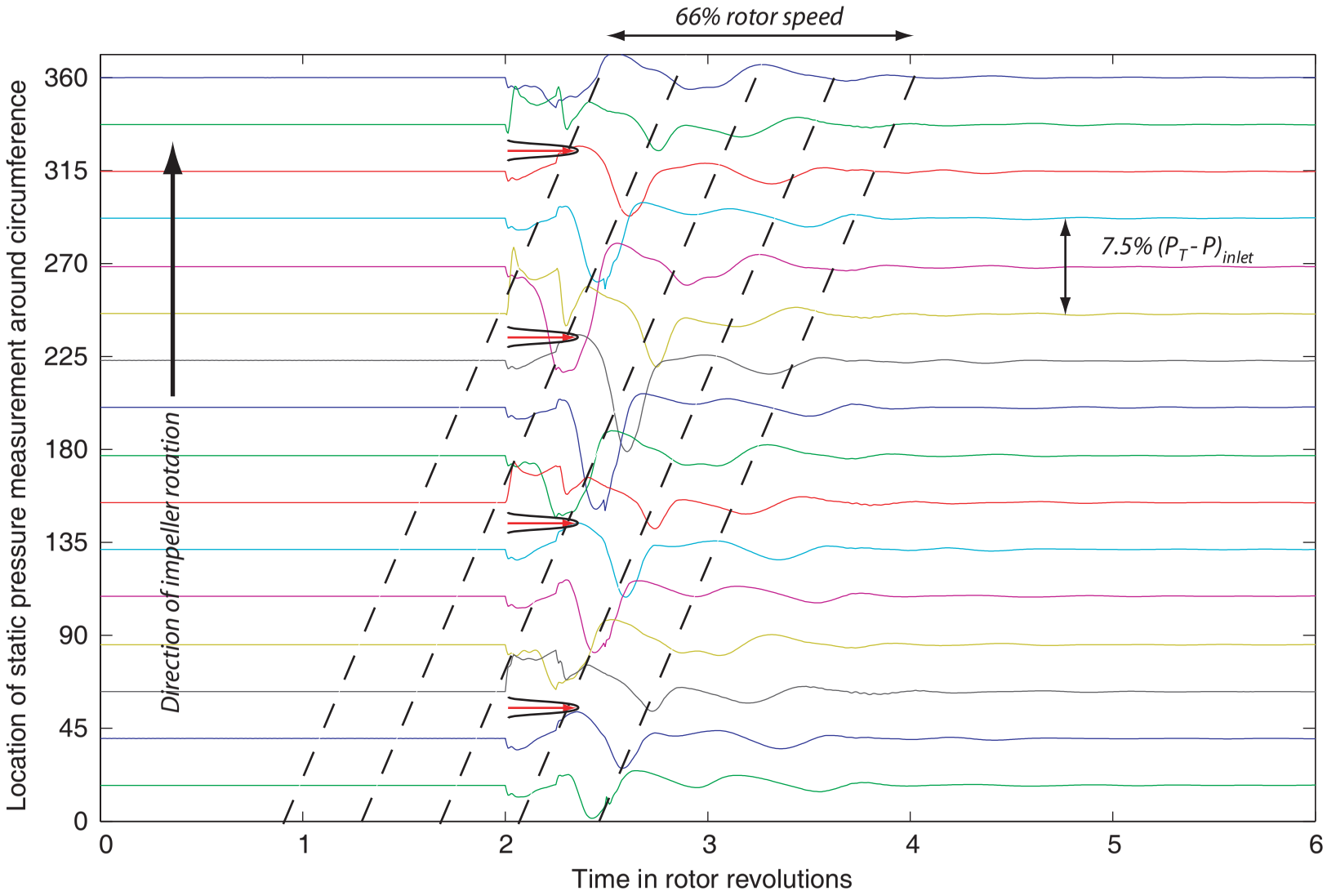

Figure 3-17: Static pressure traces in the vaneless space for unsteady test case B, repeated around the circumference to illustrate disturbance propagation.

front rotates 360 degrees in 1.5 rotations, or the disturbance is traveling at approximately 66% rotor speed. This is faster than the speed of the spike observed in [20], which traveled at approximately 15% rotor speed.

3.3.3 Backward-traveling Wave-like Disturbances in the Vaneless Space

In addition to the dominant forward-traveling spike-like disturbance, a weaker, backward-traveling disturbance is also evident in the unsteady traces. This "wave-like" disturbance appears at approximately 3 rotations in Figure 3-15, and can be seen to rotate opposite the direction of the rotor rotation. The backward-traveling wave-like disturbance persists for approximately 1.5 rotations in case B.

The same traces plotted in Figure 3-17 are used to analyze the backward-traveling disturbance in Figure 3-18. This figure shows that one wave front rotates 360 degrees in approximately 2-1/3 rotations, corresponding to a rotation speed of approximately 43%. Also, the backward-traveling wave first appears at approximately 90 degrees on the circumference, which is near the edge of the quarter-circumference's computational domain. This suggests that the backward-traveling disturbance may be caused by interaction of the forward-traveling disturbance against the periodic boundary, but further study of the wave's origin is necessary to confirm whether the origin of the disturbance is a numerical or physical issue.

3.4 Summary

In this chapter a framework was outlined for an unsteady, single blade-row, multi-passage radial vaned diffuser simulation. The framework was able to simulate rotating disturbances by means of a localized forcing in total pressure, which represents a first simulation of rotating short-wavelength disturbances in a radial vaned diffuser. Further analysis of the rotating disturbances suggested a decreased degree of damping in the vaneless space as diffuser exit pressure was increased, which is in agreement

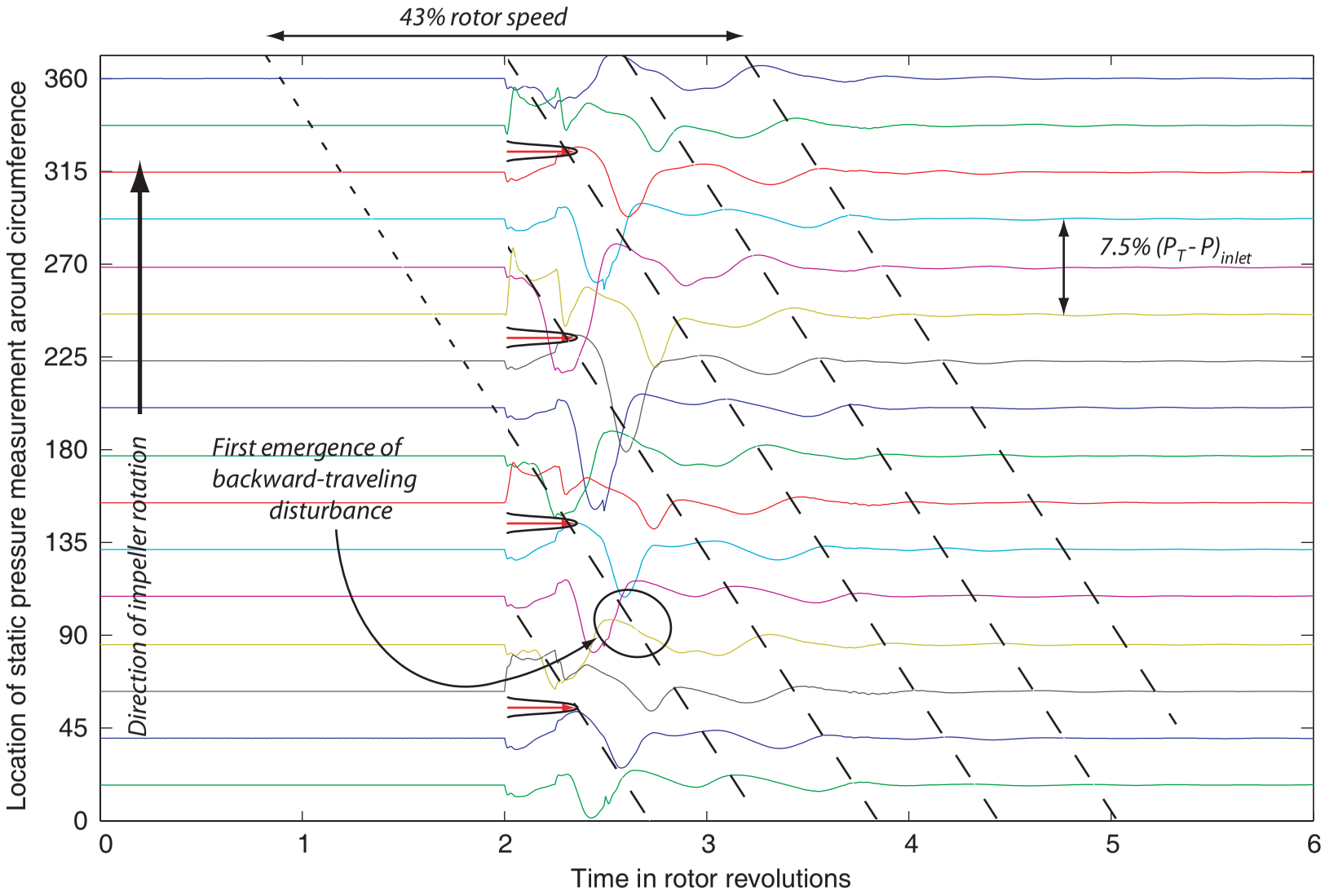

Figure 3-18: Static pressure traces in the vaneless space for unsteady test case B, for the locations at 22.5, 45, 67.5 and 90 degrees, repeated around the circumference.

with experimental unsteady stall ramp measurements.

Additionally, analysis of the unsteady static pressure response of the vaneless space to the forced input suggests local differences in the damping, which through future investigation may lead to an improved understanding of the origins of stall inception.

Chapter 4

Conclusions

This thesis describes two sets of numerical simulations performed on an advanced centrifugal compressor stage with a vaned diffuser.

The first was a steady simulation of the compressor stage with the goal of evaluating the effects of leakage flow at impeller exit on stage performance. The overall stage and individual subcomponent performance was compared with experimental data, and a detailed investigation of the flow features in the diffuser was carried out.

The second was an unsteady simulation of four passages of the vaned diffuser only with the goal of assessing the dynamic response of the diffuser to a short-wavelength forcing input. An array of simulated unsteady pressure transducers was used to analyze the changes in dynamic behavior of the diffuser as the mass flow was decreased.

4.1 Major Conclusions and Findings

The steady compressor stage simulation was unable to reproduce the changes in overall and individual subcomponent performance due to leakage flow bled at impeller exit. This discrepancy is suggested to come from one of several sources: The mixing plane utilized in the calculation fails to fully capture the impeller-diffuser interaction, in agreement with previous studies. One reason for this is deemed to be the lack of the unsteady effects present in impeller-diffuser row interactions. Additionally, the cavity at impeller exit from which the leakage flow is bled was not modeled in the

simulations, and is thought to affect the diffuser inlet flow due to a modification of the recirculation through the bleed slot due to leakage flow at impeller exit.

The unsteady diffuser-only calculation was able to simulate rotating disturbances to the quasi-steady diffuser flow by means of a short wavelength forcing in total pressure. This process comprised a new diffuser-only approach to assessing dynamic response and stall precursors in radial vaned diffusers. The disturbances were formed without the presence of tip leakage flow as it occurs in the rotors of axial compressors. Analysis of the unsteady pressure response of the diffuser to the forcing indicated a higher amplitude in the static pressure response as the exit pressure increased and mass flow decreased. This is in agreement with several experimental stall ramp measurements of centrifugal compressors. The details of the origin and nature of the rotating disturbances need to be investigated in further work, as time constraints limited their analysis in this thesis.

4.2 Future Work

The two types of simulations investigated in this thesis identified several topics for further study:

- The steady compressor stage simulation was limited by stability issues due to the exit static pressure boundary condition. A simulation utilizing mass flow as the exit static pressure may be capable of modeling the flow in the compressor stage beyond the peak of the compressor characteristic.

- Analysis of the mixing plane approach indicated that the circumferential component of the static pressure gradient at the mixing plane is ignored by the mixing plane implementation. A mixing plane implementation that can model this component of the diffuser flow field may be capable of better modeling the impeller-diffuser interaction without an unsteady calculation.

- The cavity at impeller exit was not modeled in the stage simulations. This is suggested to have a significant effect on the flow field in the vaneless space and

vaned diffuser. An unsteady simulation of the full circumference including the impeller exit cavity is currently being carried out to investigate the impact of this recirculation on the flow field in vaneless space and vaned diffuser.

- The framework described to execute the unsteady simulation of the diffuser only can be used to perform a parametric investigation of the effects of axial inlet flow non-uniformity on the stability and performance of the diffuser row. The literature suggests that the axial non-uniformity plays a key role in the diffuser performance, but it is not fully understood what degree of diffuser inlet non-uniformity is necessary to destabilize the flow in the diffuser.

- The unsteady diffuser calculations used four of sixteen vaned-diffuser passages, limiting the possible frequencies in the response of the diffuser. An unsteady diffuser calculation of all sixteen vaned-diffuser passages could be carried out to model long wavelength disturbances in the diffuser flow field and can investigate the effects of leakage flow on the dynamic compressor behavior. Additionally, a simulation of the full diffuser circumference can address the origin of the backward-traveling disturbance discussed in Chapter 3. A full diffuser circumference calculation would eliminate the need for a periodic boundary condition, which is suspected to form the backward-traveling disturbance through by reflection.

Bibliography

[1] T. R. Camp and I. J. Day. A study of spike and modal stall phenomena in a low-speed axial compressor. *ASME J. of Turbomachinery*, 120:393–401, 1998.

[2] N.A. Cumpsty. *Compressor Aerodynamics*. Krieger Publishing Company, 2004.

[3] W.N. Dawes. A simulation of the unsteady interaction of a centrifugal impeller with its vaned diffuser: Flow analysis. *ASME Journal of Turbomachinery*, 117:213–222, 1995.

[4] R.C. Dean. The fluid dynamic design of advanced centrifugal compressors, 1974. Lecture Notes, Von Karman Institute, Brussels, Mar.

[5] H. Emmons, C. Pearson, and H. Grant. Compressor surge and stall propagation. *ASME Transactions*, 77:455–469, 1955.

[6] V.G. Filipenco, S. Deniz, J.M. Johnston, E.M. Greitzer, and N. A. Cumpsty. Effects of inlet flow field conditions on the performance of centrifugal compressor diffusers: Part 1–discrete-passage diffuser. *ASME J. of Turbomachinery*, 122:1–10, 2000.

[7] E. M. Greitzer, C. S. Tan, and M. B. Graf. *Internal Flow: Concepts and Applications*. Cambridge University Press, 2005.

[8] Squire H.B. and Winter K.G. The secondary flow in a cascade of aerofoils. *Journal of Aero Science*, 18:271, 1951.

[9] J. Horlock, P. Percival, J. Louis, and B. Lakshminarayana. Wall stall in compressor cascades. In *ASME Fluids Engineering Division, Winter Annual Meeting, New York*, 1964. Paper 64-WA / FE-29.

[10] R. Hunziker and G. Gyarmathy. The operational stability of a centrifugal compressor and its dependence on the characteristics of the subcomponents. *ASME J. of Turbomachinery*, 116, 1994.

[11] V.M. Lei, Z.S. Spakovszky, and E. M. Greitzer. A criterion for axial compressor hub-corner stall. To appear in *ASME Journal of Turbomachinery*, 2007.

[12] B.A. Leishman and N.A. Cumpsty. Mechanism of the interaction of a ramped bleed slot with the primary flow. In *Proceedings of ASME TURBO EXPO 2005*, June 2005. Paper GT2005-68483.

[13] N.M. McDougall, N.A. Cumpsty, and T.P. Hynes. Stall inception in axial compressors. *ASME Journal of Turbomachinery*, 112:116–125, 1990.

[14] F.K Moore and E.M. Greitzer. A theory of post-stall transients in axial compressors, part I - development of equations. *ASME Journal of Engineering for Gas Turbines and Power*, 108:68–76, 1986.

[15] Numeca International, 5 Avenue Franklin Roosevelt, Brussels BELGIUM. *FINE^{TM}/Turbo User Manual Version 7a.*

[16] M. Peeters and M. Sleiman. A numerical investigation of the unsteady flow in centrifugal stages. In *Proceedings of ASME TURBO EXPO 2000*, June 2000. Paper 2000-GT-426.

[17] L. Reneau, J. Johnston, and S. Kline. Performance and design of straight, two-dimensional diffusers. *ASME J. of Basic Engineering*, 89:141–150, 1967.

[18] Niklas Sievers. Personal communication, 2006.

[19] Z.S. Spakovszky. Backward traveling rotating stall waves in centrifugal compressors. *ASME Journal of Turbomachinery*, 126:1–12, 2004.

[20] Z.S. Spakovszky and C.H. Roduner. Spike and modal stall inception in an advanced turbocharger centrifugal compressor. *Proceedings of ASME TURBO EXPO*, 2007.

[21] A. Stein, S. Niazi, and L.N. Sankar. Numerical analysis of stall and surge in a high-speed centrifugal compressor. AIAA Paper 2000-0226, January 2000.

[22] A. H. Stenning. Rotating stall and surge. *ASME J. of Fluids Engineering*, 102:14–20, 1980.

[23] T. Yoshinaka. Surge responsibility and range characteristics of centrifugal compressors. *Tokyo Joint Gas Turbine*, 1977.